Escola Tècnica Superior d'Enginyeria de Telecomunicació de Barcelona

UNIVERSITAT POLITÈCNICA DE CATALUNYA

ICFO

Institut de Ciències Fotòniques

Design and development of a portable cytometer based on image sensor technology

Master Thesis

Author:
Eng. Juan Miguel Pérez Rosas

External Supervisor:
Prof. Valerio Pruneri
Co-Supervisor:
PhD Marc Jofre
Internal Supervisor:
Prof. Maria Concepción Santos

A thesis submitted in fulfillment of the requirements for the Master in Telecommunications Engineering in the

Universitat Politècnica de Catalunya

ETSETB

September, 2014

Abstract

This Thesis focuses on the development of the opto-mechanical design and software interface of an image cytometer capable of analyzing particulate in a small volume sample. The device consists of an incoherent light source, a CMOS image sensor to digitize the sample information and optical elements which retrieve the complete complex Fourier transform of the specimen's wave front and optically process it for detection. Both brightfield and fluorescence implementations are investigated and demonstrated to be functional for the detection, identification and characterization of mixed particulate compositions in the same volume, over a broad range of specimen concentrations (10^7CFU/ml – 10^2CFU/ml).

The Thesis includes an in depth study of the state-of-the-art in related fields, in particular the technologies exploited to construct the prototype. It then describes the design and the development of the image cytometer and the related software for signal processing and sample analysis, from an initial lab demonstrator to a pre-industrial device that can be used for experiments in real settings (hospitals, food production lines, water installments, etc…).

The developed image cytometer, very compact and potentially low cost, has been used to detect several cells and microorganisms related to the health diagnosis (infectious diseases), food industry and environmental analysis. These include Jurkat and K562 cells, streptococcus, Bordetella and E. coli microorganisms to levels comparable to those detected by more traditional and cumbersome methods, such as those relying on large flow cytometry equipment.

Resumen

Ésta Tesis se enfoca en el desarrollo del diseño opto-mecánico y la interfaz de software de un citómetro de imagen capaz de analizar partículas en pequeños volúmenes de muestra. El dispositivo consiste en una fuente de luz incoherente, un sensor de imagen CMOS para digitalizar la información de la muestra y elementos ópticos que obtienen la transformada compleja de Fourier del frente de onda del espécimen y la procesan para su detección. Implementaciones tanto no-fluorescentes como fluorescentes han sido investigadas y se ha demostrado su funcionalidad para la detección, identificación y caracterización de composiciones mixtas de partículas en un mismo volumen, sobre un amplio rango de concentraciones del espécimen (10^7UFC/ml – 10^2UFC/ml).

La Tesis incluye un estudio profundo del *"state-of-the-art"* en campos relacionados, en particular las tecnologías explotadas para la construcción del prototipo. Luego describe el diseño y desarrollo del citómetro de imagen y el software asociado para el procesado de la señal y el análisis de la muestra, desde un prototipo inicial de laboratorio hasta un dispositivo pre-industrial que puede ser utilizado en escenarios reales (hospitales, líneas de producción de alimentos, depósitos de agua, etc…).

El citómetro de imagen desarrollado, muy compacto y potencialmente de bajo coste, ha sido utilizado para detectar células y microorganismos relacionados al diagnóstico de enfermedades infecciosas, la industria alimenticia y estudios ambientales. Estos incluyen células Jurkat y K562, microorganismos estreptococos, Bordetella y E. coli a niveles comparables a los detectados mediante métodos más tradicionales y engorrosos, como aquellos que requieren el uso de equipos de citometría de flujo de gran tamaño.

Resum

Aquesta Tesi s'enfoca en el desenvolupament del disseny opto-mecànic i la interfície de programari d'un citòmetre d'imatge capaç d'analitzar partícules en petits volums de mostra. El dispositiu consisteix en una font de llum incoherent, un sensor d'imatge CMOS per digitalitzar la informació de la mostra i elements òptics que obtenen la transformada complexa de Fourier del front d'ona de l'espècimen i la processen per a la seva detecció. Implementacions tant no-fluorescents com fluorescents han estat investigades i s'ha demostrat la seva funcionalitat per a la detecció, identificació i caracterització de composicions mixtes de partícules en un mateix volum, sobre un ampli rang de concentracions de l'espècimen (10^7UFC/ml – 10^2UFC/ml).

La Tesi inclou un estudi profund del "*state-of-the-art*" en camps relacionats, en particular les tecnologies explotades per a la construcció del prototip. Després descriu el disseny i desenvolupament del citòmetre de imatge i el programari associat per al processat del senyal i l'anàlisi de la mostra, des d'un prototipus inicial de laboratori fins a un dispositiu preindustrial que pot ser utilitzat en escenaris reals (hospitals, línies de producció d'aliments, dipòsits d'aigua, etc ...).

El citòmetre d'imatge desenvolupat, molt compacte i potencialment de baix cost, ha estat utilitzat per a detectar cèl · lules i microorganismes relacionats al diagnòstic de malalties infeccioses, la indústria alimentària i estudis ambientals. Aquests inclouen cèl · lules Jurkat i K562, microorganismes estreptococs, Bordetella i E. coli a nivells comparables als detectats mitjançant mètodes més tradicionals i enutjosos, com aquells que requereixen l'ús d'equips de citometria de flux de grans dimensions.

Contents

Abstract iii
Resumen iv
Resum v
List of Figures viii
List of Tables ix
1 Introduction 11
1.1 Imaging Cytometry 11
1.2 Statistical Analysis of Particulate Detection 13
1.3 Image Sensor Technology 15
1.3.1 Charged Coupled Device (CCD) 19
1.3.2 Complementary Metal-Oxide-Semiconductor (Active Pixel Sensor) 20
1.3.3 CCD and CMOS Tradeoff 22
1.3.4 High Dynamic Range Imaging 23
1.4 Lens Free Microscopy 24
1.4.1 Compressive Sampling 24
1.5 Fluorescence Microscopy 25
1.5.1 Fluorescent Microscope Novel Techniques 28
1.6 Volumetric Analysis in Image Cytometers based on Fourier Optics Principles 37
1.7 Aim of the Thesis 39
1.8 Outline of the Thesis 39
2 Imaging System 40
2.1 Exposure Time and Gain Optimization for LDR captures 40
2.2 HDR Capturing Algorithm 41
2.3 Capturing Algorithm Results and Discussion 42
2.4 Imaging System Results and Discussion 45
2.5 Summary 50
3 Optical Cytometer for Particulate Analysis in Target Specimen Volumes 51
3.1 Cytometer Design 51
3.2 Dispersion Graphs and Complexity vs. Size Analysis 52
3.3 E. coli and Mixed Size Particles Characterization 54
3.4 Bordetella bronchiseptica and Streptococcus pneumonia Characterization 56
3.5 Jurkat Cells and K562 Cells (Lymphocyte and Granulocyte) Characterization 60

3.6 Fluidics 61
3.7 Summary 63
4 Conclusions 65
References 67

List of Figures

Figure 1.1: Sort efficiency in flow cytometry techniques 15
Figure 1.2: The Bayer arrangement of color filters 16
Figure 1.3: Foveon 3X technology 16
Figure: 1.4: 3CCD cameras 17
Figure 1.5: Single pixel structure (CCD) 19
Figure 1.6: Schematic structure of CCD capture process 20
Figure 1.7: Single pixel structure (CMOS) 21
Figure 1.8: Schematic structure of CMOS capture process 22
Figure 1.9: Schematic and prototype of lens-free microscope 24
Figure 1.10: Excitation spectrum of native GFP 25
Figure 1.11: Effect of photo bleaching through a series of digital images 27
Figure 1.12: Representation of the FRET phenomena 27
Figure 1.13: Cut-away diagram of Epi-fluorescent microscope 28
Figure: 1.14: Fluorescent microscope attachment for a smartphone 29
Figure 1.15: Fluorescent microscope attachment with inclined pump 29
Figure 1.16: Resulting capture with prototype of figure 1.12 30
Figure 1.17: Schematic, experimental setup and results of lens-free fluorescent microscope 31
Figure 1.18: Experimental setup of lens-free fluorescent microscope 32
Figure 1.19: Resulting capture with prototype of figure 1.16 32
Figure 1.20: Representation of strength of compressive sampling algorithm 33
Figure 1.21: schematic of chip-scale microscope 33

Figure 1.22: Resulting capture with prototype of figure 1.19 34
Figure 1.23: Schematic of optical fluorescent sensor 34
Figure 1.24: Comparison of results between prototype of figure 1.21 and laser scanner 35
Figure 1.25: Light field microscope prototype 35
Figure 1.26: Resulting capture with prototype of figure 1.23 36
Figure 2.1: Scenes capture in the laboratory 42
Figure 2.2: Optimized LDR captured 43
Figure 2.3: Computer generated representation of sparse mask 43
Figure 2.4: Green channel capture of a sparse physical matrix 44
Figure 2.5: A pattern composed of cubic sub-structures of Titania 45
Figure 2.6: Recovered image of a particle slide 46
Figure 2.7: Recovered image of Jurkat cells 47
Figure 2.8: Recovered image E. coli 48
Figure 2.9: Sample of figure 2.8 after compressing sampling algorithm 48
Figure 3.1: Schematic and prototype of optical cytometer 51
Figure 3.3: Dynamic range of concentrations for optical cytometer 55
Figure 3.4: Dispersion graph for E. coli and particle samples 56
Figure 3.5: Dispersion graph for streptococcus and particle samples 57
Figure 3.6: Microbiological charge tendency line 58
Figure 3.7: Dispersion graph for streptococcus and Bordetella samples 59
Figure 3.8: Dispersion graph for Jurkat and K562 cells samples 60
Figure 3.9: Schematic of the fluidic system designed 62
Figure 3.10: Demo test of the fluidic system 63

List of Tables

Table 1.1: Analysis of commercial equipment and the apparatus in this work 13
Table 1.2: Probability of cell presence for a single sample and different concentrations 14
Table 1.3: Statistical estimate of cell detection in flow cytometers 14

Table 1.4: Probability of particulate presence in a sample of 8µl ……14

Table 2.1: Gain register values for CMOS sensor ……40

Table 2.2: Concentration estimates of the captured Jurkat cells ……47

Table 3.1: Statistics of fluorescence intensity images ……54

Table 3.2: Intensity values for samples over decreasing pump optical intensity ……55

Table 3.3: Series of captures represented in Figure 3.5 ……58

Table 3.4: Microbiological charge on streptococcus and Bordetella captures ……59

Table 3.5: Microbiological charge on Jurkat cells and K562 ……44

1 Introduction

An overall review of the cytometry market, towards which the prototype of this work is intended, is presented; along with a detailed review of the technologies that took part in the development of the device as well as an insight into the state of the art. The key element in an image cytometer is the light detector; therefore a review of image sensing technologies as well as their comparative study will be presented. Lens free microscopy is introduced, as it is the starting technology for the designed device. In order to assert the relevance and innovation of this work, an examination on the advances in the field published by top level universities and institutions is performed. Finally an introduction to the Fourier optics principles is given since said principles are key to understanding the disclosed apparatus.

1.1 Imaging Cytometry

A system that can rapidly process and measure cells, particles or microorganisms is a high necessity in life sciences research, food industry, environmental monitoring, pharmaceutical drug discovery and clinical diagnostics. Early detection is critical for the effective treatment and prevention of diseases. In many cases, diagnosis unfortunately requires time-consuming and costly procedures and instruments, which limits their use to centralized settings with relatively advanced infrastructures and well-trained healthcare professionals [1]. Lens-based epifluorescence microscopes have long been standard equipment in biological imaging despite their inherent disadvantages of high cost, large size, and limited field of view (FOV) [2]. Within the food industry bacterial cell culture-based methods are considered the gold standard by the food and drug administration (FDA) for detection of pathogens in food [3]. However with this method, the presence of E. coli in food specifies culture plate confirmation after 48 to 56 hours. In biological applications, it takes several hours or days even today until the physician receives the results [4]. With the recent advances in opto-electronic components as well as computational resources having better processors and more sophisticated algorithms, lens free on-chip imaging is becoming an important alternative to conventional lens-based microscopy for both bright-field and fluorescent imaging. This is a rather important step-forward for telemedicine based fluorescent microscopy, which could especially be valuable for diagnosis of infectious diseases such as tuberculosis [5]. Over the last decade a great deal of research has been dedicated to the development of biological sensors for the detection of microorganisms allowing rapid “real-time” identification. These biosensors can be classified in four basic groups depending on the transduction method: optical, mass, electro-chemical and thermal [6]. Biosensor technologies rank fourth in the area of pathogen detection; with optical transduction having the highest percentage (35%) of usage in biosensors [7]. Optical technologies can be very powerful when it comes to detecting minute quantities of biomarkers with the purpose of measuring and/or evaluating biological and pathogenic processes. More specifically, microscopy can be combined with fluorescence based labelling and detection to achieve biomedical testing platforms, routinely used by large laboratories and clinics. The use of antibody based sensors permit the rapid and sensitive analysis of a range of pathogens and associated toxins [8]. On the past few years, interest has risen on finding more appropriate solutions to the market needs, by

making use of low cost imaging technologies based on charged coupled device (CCD) or complementary metal-oxide semiconductor (CMOS) image sensing.

Flow cytometry is a matured technology that has lately experienced significant growth and innovation. This analytical laboratory technique can rapidly measure different parameters on single cell or particle with strong reliability. Even though the global flow cytometry market remains one of the fastest growing segments in life sciences [9], market trends continue evolving as new applications, devices and systems are developed. One of the most significant applications of flow cytometry relies on clinical diagnosis; however the field is facing budgetary constraints from payers and providers as the impact of such expensive technologies is not always justified for preclinical and biomedical laboratories. In most of these cases, the use of core facilities is approached; however the need for fastest diagnostics and clinical decisions motivated the search for novel more cost efficient solutions. Advances CCD have great potential in lowering prices by substituting expensive laser sources with much cheaper, up to two orders of magnitude, light-emitting diodes and sophisticated microscopes with simple and more economic proximity detection schemes. These image cytometers can be easily operated through direct cell imaging on a computer screen. Unlike flow cytometers, image cytometers don't measure illuminating the cells with a laser one by one but takes an image of cells arranged on a microscope slide and analyzes thousands of cells in a single picture [9]. For these reasons image cytometers are entering gradually into the market as they offer similar characteristics and benefits to the classic flow cytometers but at lower cost.

An effort has been made by the research community that resulted on emerging new technologies that can erode the cytometry market. A silo-filter CMOS for a chip-scale fluorescent microscope has been demonstrated reaching a spatial resolution of 10µm over a 6mmx4mm FOV [2]. A lens less fluorescent microscope with a FOV of approximately 60mm^2 and spatial resolution of under 4µm has been designed using a fiber optic faceplate to conduct the fluorescence emission and a prism surface to reflect the excitation wavelength [10], [11]; the spatial resolution is achieved by applying compressive sensing techniques over the captured image by knowing the system's response. A compact cell-phone attachment has been proven to work for dark-field imaging using a lens-system that achieves a FOV of about 80mm^2 with spatial resolution of 20µm [5], [12], [13].

Other techniques have been developed to increase the depth of field (DOF) of the sample volume to analyze and enhance the sensitivity of the devices. Micro lens arrays have been used in this sense to build a single view-point microscope that results in an ultra-wide FOV [14]. They are also used as one of the key elements of Light Field Microscopy which is a multi-view point imaging technique that can be resolved by applying three-dimensional convolution algorithms to captured samples with a large DOF [15]–[17]. Other approach has been to employ the micro array to improve the Signal to Noise on measurements, ultimately demonstrating an optical sensor for fluorescence quantification [4].

Yet another approach has been to capture amplitude and phase images synthetized from a set of Fourier holograms. Each hologram records a region of the complex two-dimensional spatial frequency spectrum of an object [18].

In this work, an optical system capable of analyzing particulate within a target specimen volume, both in terms of FOV and DOF is presented. The principle behind the system is the far-field detection

and analysis of a spatial Fourier transform of the specimen's wave front focused in a set of sub-images onto a CMOS image sensor. The CMOS digitalizes the data for processing; the captured data contains information on both amplitude and phase of the sample's transform (the complete complex Fourier transform). This provides the basis of an image cytometer that performs sample analysis in the Fourier domain. A system capable of analyzing the structure, shape and size of cells, particles or microorganisms contained in a target specimen volume is demonstrated as well as statistical counting of the particles in said volume for concentration estimates.

The apparatus designed shows an increase in analyzed sample volumes resulting in both improved concentration precision, dynamic range and identification of different particulate families. The thesis also includes a novel methodology to analyze the sample in the spatial frequency domain ultimately retrieving information on shape, size and structure of the particulate within the sample. It is also shown how the device is capable of operating on both dark field for fluorescently marked samples and bright field for unmarked specimens.

Before entering into the details of the apparatus' design and characterization, some theoretical aspects of the technologies employed as well as the state of the art are reviwed.

1.2 Statistical Analysis of Particulate Detection

The Technical requirements and expected goals for cytometry devices aimed at biological and environmental measurements are shown in Table 1.1. The table shows a comparative analysis of current commercial equipment against the apparatus developed within this thesis. The goal is a sample volume of approximately 1ml obtained through the use of 1l to 1ml concentrators. An absolute counting range for the fluorescent particulate from 10^7CFU/ml to 10^2CFU/ml with a detection limit of 10CFU/ml and a 0.5 logarithmic concentration precision.

Technical parameter	Current commercial equipment	Developed Optical Cytometer
Sample volume analysis	600ul-800ml	1ml-3ml (use of 1l to 1ml concentrator)
Particulate fluorescently marked absolute counting range	10^7CFU/ml - 10 CFU/ml	10^7CFU/ml – 10^2 CFU/ml
Detection limit	-	10 UFC/ml
Counting concentration precision	0.5 log	0.5 log
Fluorescence channels	>2	2
Measurement time	<15 minutes	<15 minutes
Fluidic system	-	TBD (pump, concentrator and sample). Auto-cleaning cartridge.

Table 1.1. Comparative analysis of current commercial equipment against the apparatus developed within this work. The goal is a sample volume of approximately 1ml obtained through the use of 1l to 1ml concentrators. An absolute counting range for the fluorescent particulate from 10^7CFU/ml to 10^2CFU/ml with a detection limit of 10CFU/ml and a 0.5 logarithmic concentration precision.

A biological cell sample it is known to follow a Poisson distribution in terms of event occurrence within a sample (Colony Forming Unit - CFU); this means that given a concentration and a sample volume, CFU's present in the sample can be accurately estimated. CFU counting also follows a predictable behavior when approach with cytometry techniques. Table 1.2 summarizes the theoretical optimum performance of a flow cytometer capable of analyzing the whole sample in question.

CFU per Sample	1	10	100	1000	10000
% of total CFU sorted	100	99,9	98,5	86,1	22,3
% of samples with 1 or more cells	63,2	100	100	100	100

Table 1.2. Probability of total cells sorted and probability of one or more cells presence for a single sample and different concentrations.

For a sample volume of 2ml processed through flow cytometry at a period of nearly 11 drops/sec, the statistical estimate of CFU detection in terms of concentration follows the data in Table 1.3.

Concentration (CFU/ml)	10^1	10^2	10^3	10^4	10^5	10^6	10^7	10^8	10^9	10^{10}
% CFU Detected	100	100	99.4	98.5	94.4	86.1	57.6	36.1	22.3	5.6

Table 1.3. Typical statistical estimate of cell detection in flow cytometers at a period of nearly 11 drops/sec.

For an image cytometry system, the probability of particle presence in a sample of 8µl given a certain concentration of particles per ml will follow a Poisson distribution represented in Table 1.4. The probability of presence of 0 and 1 particles is shown as well as the probability of 1 or more particles in general. The process of loading the sample is independent, thus the probabilities of multiple events are obtained by additive result.

Concentration (CFU/ml)	Probability of Zero Cells in 8µl	Probability of One or more Cells in 8µl	Probability of One Cell in 8µl
1	99.2	0.79	0.79
10	92.3	7.68	7.38
100	44.9	55.06	35.9
1000	0.03	99.9	0.26
10000	0	100	0

Table 1.4. Probability of particulate presence in a sample of 8µl for different concentrations in ml.

In flow cytometry techniques, the sort efficiency (CFU counting) is inversely proportional to the amount of particulate in a sample which in turn implies its concentration, as shown in Figure 1. 1.1.

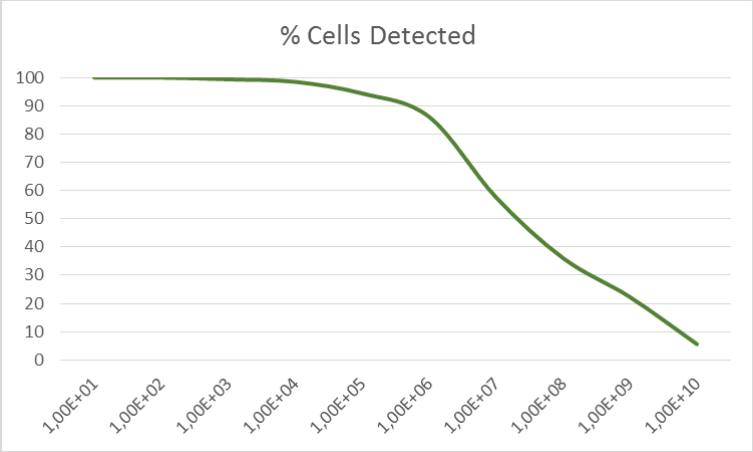

Figure 1.1. In flow cytometry techniques, the sort efficiency (cell counting) is inversely proportional to the amount of cells in a sample. The vertical axis shows the sorting percentage, meaning the number (%) of particulate differentiated and counted.

1.3 Image Sensor Technology

An image sensor is a device capable of converting an optical image into an electrical signal [19]. Among current technologies there are CCD, active pixel sensors (CMOS) and its second generation the scientific CMOS (sCMOS). Before detailing these three technologies, a view on two major factors of image sensors is taken; the color separation mechanism and the noise parameters in an image sensor.

A common classification of image sensors is by the color separation mechanism implemented. Three main mechanism are well implemented in today's technologies. The Bayer filter sensor, the Foveon X3 sensor and the 3CCD [20].

The Bayer Filter sensor is the most common and low-cost solution to the color separation issue. It uses a color filter array that passes red, green or blue light to independent pixel sensors. The filter is an interlaced grid of these pixel sensors. The missing colors are interpolated from the collected data. The filter patter is 50% green, 25% red and 25% blue, which means there are twice as many green pixel sensors as there are red or blue. Figure 1.2 shows the pixel array of an arbitrary image sensor. A modification of the Bayer filter uses a grid of four different pixels; the usual red, green and blue and in addition a panchromatic cell which is sensitive to all visible light wavelengths. The sensor is commonly referred to as RGBW (Red, Green, Blue and White) [21].

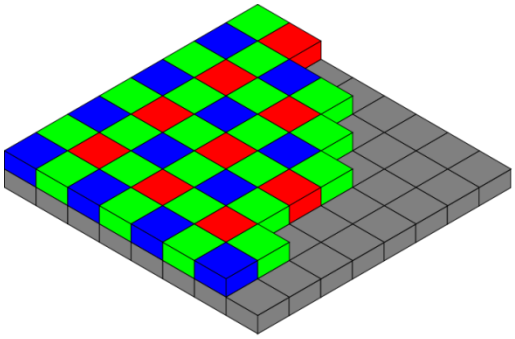

Figure 1.2: The Bayer arrangement of color filters on the pixel array of a given image sensor. The 50% green, 25% red and 25% blue pattern is evident [21].

The Foveon X3 is a technology that uses a vertical array of layered pixel sensors. Each array consists of three pixel sensors stacked vertically and a set of these arrays are setup in matrix form to build up the whole sensor. Each of the pixels within the array are sensible to a different wavelength (RGB), the remaining colors are interpolated similarly to the Bayer filter. The idea behind the design is to be able to construct a sensor capable of detecting all three wavelengths over all its surface contrary to the Bayer filter implementation [22].

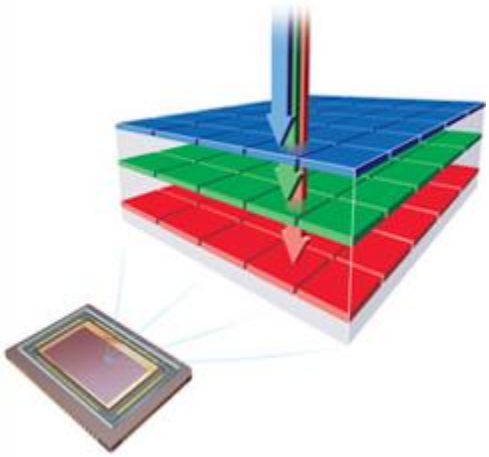

Figure 1.3: Foveon X3 technology. It uses a vertical array of layered pixel sensors. Each array consists of three pixel sensors stacked vertically and a set of these arrays is setup in matrix form to build up the whole sensor. Each of the pixels within the array are sensible to a different wavelength (RGB) [22].

The 3CCD cameras use a set of three CCD's to detect each one of the primary colors (RGB). By taking separate readings the precision of the device and the effective resolution of the resulted image is significantly higher than image sensor using a single sensor and Bayer filter combination mechanism. However the cost of the device is also generally higher and the implementation of the technology is more difficult. Firstly a tri-chroic prism assembly is needed prior to the sensor to accordingly direct the incoming wavelengths to sensors. After detection a recombination mechanism is also necessary and achieved by aligning the sensors [23].

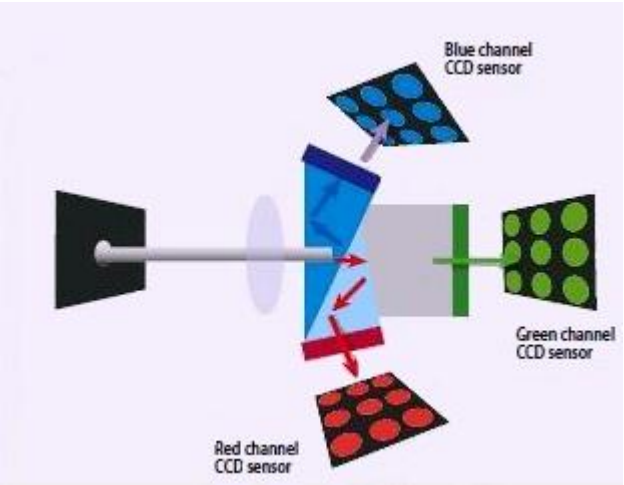

Figure 1.4: 3CCD cameras. It uses a set of three CCD's to detect each one of the primary colors (RGB). By taking separate readings the precision of the device and the effective resolution of the resulted image is significantly higher than image sensor using a single sensor and Bayer filter combination mechanism [23].

Another significant parameter in image sensor technologies is noise within the captured signal; just as it is in every signal processing or communications system in general. There is an inner classification of the noise present when capturing images with any image sensor. It can be classified in shot noise, read noise, dark noise and fix pattern noise; all of these are described next.

Shot Noise

Shot noise is a type of electronic noise linked to the discrete nature of the electric charge. More specifically, shot noise is the random phenomenon created by the movements of electrons within an electrical current causing said current to suffer fluctuations. In many cases shot noise is rendered insignificant since the random movements of the electrons cause fluctuations of several orders below the actual electrical current. This however is not the case for optoelectronic devices like image sensors; in this type of devices the shot noise is inherently linked to the random detection of photons. When photons are detected by an optoelectronic device with a quantum efficiency below unity this process of conversion becomes a relevant factor that leads to an increase in the shot noise level. In the context of optics is also known as quantum noise or photon noise. In an image sensor the shot noise (N_{shot}) can be quantized as a function of the exposure time (t_{exp}), the quantum efficiency (η) and the photon flux (P) (see Equation 1.1).

$$N_{shot} = \sqrt{P \cdot \eta \cdot t_{exp}} \tag{1.1}$$

Read Noise

It is also an electronic noise of Gaussian nature. For active pixel sensors (CMOS, sCMOS) it is proportional to the inverse of the capacitance of the read transistor gate. It is in nature an additive noise and independent at each pixel. It is also independent of the input signal as it is uniquely related to the sensor's inner electronics. It can be said that the read noise scales down as pixel area increases, since for planar structures (as pixels are) the capacitance is proportional to the area.

Dark Noise

It is a type of noise associated with the sensor's dark current; this is the current detected by the sensor even when no incident photons are present. This current contributes to two kinds of noise. A dark offset which is an intrinsic offset level in the electrical current produced by the sensor, such offset is partially correlated between the pixels. The other contribution is the shot noise associated to the dark offset, in this case it is uncorrelated between pixels and can be approximated to the product of the dark current times the exposure time. In image processing it is common to obtain a mean value of the dark offset and to rectify the captured image by subtracting off said mean; however the shot noise associated is still a limiting factor since it is difficult to determine due to its random nature.

Fix Pattern Noise

This is a phenomenon present in digital image sensors present at larger exposure time where single pixels can be susceptible to give out a high level of intensity above the general background (level not present in the captured image). The name comes from the pattern created in the captured image by the set of these pixels, said pattern is in nature a temporally constant non-uniformity (hence the fix). The causes for the noise pattern are two non-uniform responses. The first is the Dark Signal Non-Uniformity (DSNU) which is an offset from the average for a particular setting of exposure time that may also be linked to temperature conditions, but in any case the response is given with no external illumination. The second is the Photo Response Non-Uniformity (PRNU) which in essence describes the gain ratio between the actual optical power and the altered electrical signal output. In general this non-uniformities are negligible for medium to short exposures; however they increase for long exposure times to the point of becoming a visible defect and degrading the resulting quality of the detected image.

For all the described noise sources, the common factor is their dependence on exposure time; therefore a more detailed look at this parameter becomes a must.

Exposure Time

It is referred to the integration time for the sensor to capture a particular image. More specifically it determines the length of time the camera's shutter will be open while taking a single capture. Therefore it is directly proportional to the amount of light reaching the sensor's surface. Such relation is given in equation 1.2.

$$\hat{\mu}_x = P \cdot \eta \cdot t_{exp} \tag{1.2}$$

Where $\hat{\mu}_x$ refers to the illumination reaching the image sensor while the other parameters were defined above (equation 1.1). Consequently, for a given sensor quantum efficiency and photon flux, the actual illumination value detected at the sensor can be tuned by setting the exposure time [24]–[26].

1.3.1 Charged Coupled Device (CCD)

CCD is a device based on the movement of electrical charges within bins of the device itself to a point they can be manipulated, usually this means being digitized. In digital imaging, CCD is used to create image sensors in which pixels are represented by a metal oxide semiconductor capacitor that being biased for inversion allows the conversion of incident photons into electrical charges (electrons) and then the CCD structure is used to transport and read out said charges.

Digital Image sensors incorporating a CCD detector are the most employed technology in modern optical microscopy. A CCD photon detector is a silicon wafer divided into several (thousands or millions) geometrically regular light sensitive regions (pixels) that capture and store image information in the form of electrical charges proportional to the incident light intensity. A CCD imager consists of a large number of pixels arranged in a two-dimensional array on a thin silicon substrate. The semiconductor properties of silicon allow this array to trap and hold photon-induced charge carriers under appropriate electrical bias conditions. The fundamental light-sensing unit of the CCD is a Metal Oxide Semiconductor (MOS) capacitor operated as a photodiode and storage device, whose reverse bias operation allows the transport of the electrical charges to an area underneath the positively charge gate.

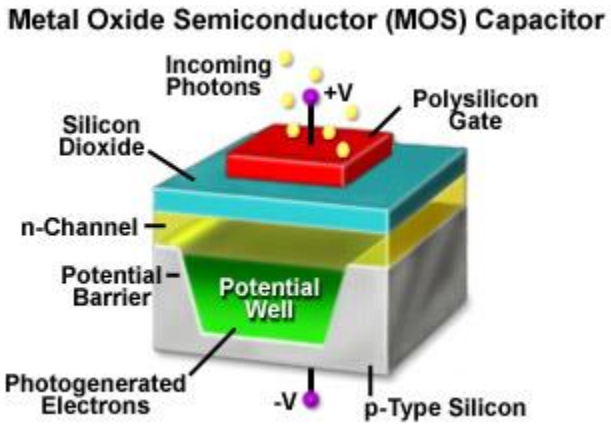

Figure 1.5: Single pixel structure consisting of a MOS capacitor. The photons are incident on the positively charge surface and the charges generated travel to the potential well to be digitalize at a later stage [27].

Figure 1.5 displays a single pixel structure consisting of a MOS capacitor. The photons are incident on the positively charge surface and the charges generated travel to the potential well to be digitized at a later stage. This photoelectrons stored inside the well can be accumulated for long periods of time (related to the device's exposure time) before being read by the camera electronics as one single capture. The image generation within a CCD can be structured in four sequential stages.

The first is the charge generation. This is the process at which the photoelectrons are generated through the interaction of the photon with the device's photosensitive region. The second stage is the collection and storage of the generated charges; at this stage the charges travel to the potential well where they are stored for further processing. The third stage consists on the transfer of the charges to the electronic Analog to Digital (ADC) stage of the sensor. The read out or measurement

of the charges by the ADC constitutes the fourth stage of the image generation. At this point the image can be recreated by a computer into three known image formats (JPG, TIFF and BMP).

In general the stored charges have a linear relation to the photon flux and the exposure time, as seen in equation 1.2. However there's a limit to this sensor linearity which is the linked to the capacity of the well. This parameter is known as Full-Well Capacity (FWC) and it determines the maximum signal that can be detected in the pixel and as will be explained later it impacts the sensor's dynamic range [27].

Figure 1.6 displays a schematic structure of the process the image sensor follows for every capture. Starting from charge accumulation during the exposure time, going through the respective register in order to correctly read the charge information at each pixel and finally obtaining an image file that can be displayed in a visual format as well as clearing the device's registers of any residual information to perform the following capture.

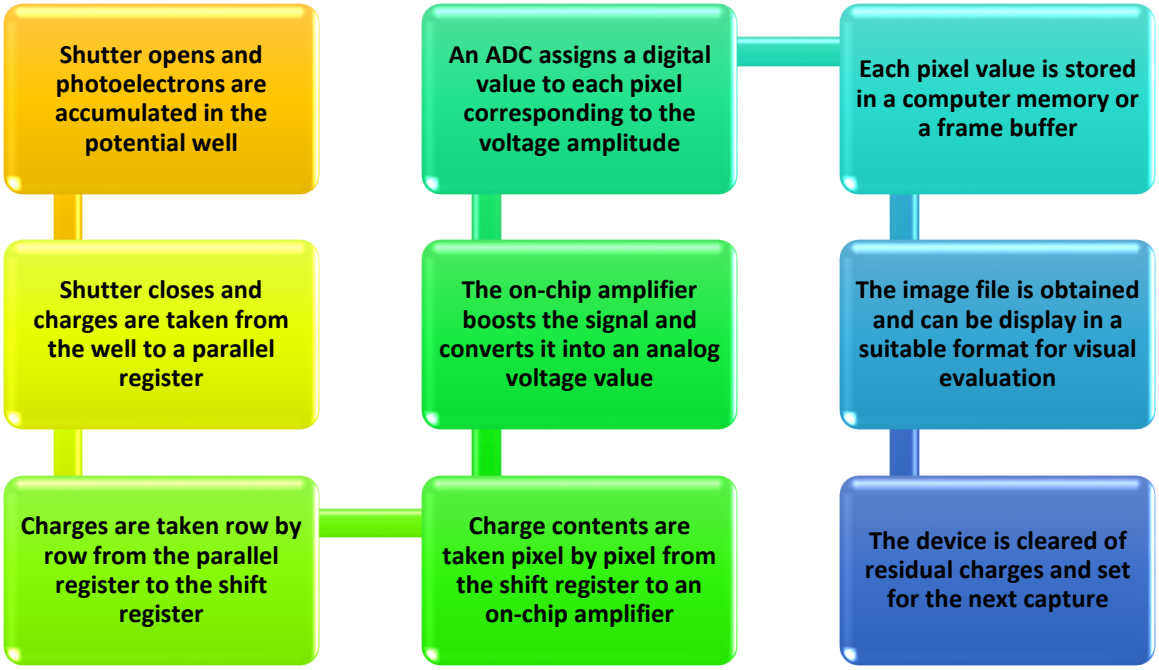

Figure 1.6: Schematic structure of the process the image sensor follows for every capture. Starting from charge accumulation during the exposure time, going through the respective register in order to correctly read the charge information at each pixel and finally obtaining an image file that can be displayed in a visual format as well as clearing the device's registers of any residual information to perform the following capture.

1.3.2 Complementary Metal-Oxide-Semiconductor (Active Pixel Sensor)

CMOS is, in the general sense, a technology to construct integrated circuits. It is based on a complementary implementation of both p-type and n-type Metal Oxide Semiconductor Field Effect Transistors (MOSFET), which consequently renders a low static power consumption and high noise immunity on the integrated circuit. This technology has a broad field of applications in the digital world for designing and producing electronic devices based on electronic logic (logic gates). In the

optoelectronics industry CMOS technology has also gather great interest as it can be implemented to produce active pixel image sensors.

An active pixel sensor is an image sensor consisting of an array of pixel sensors which in addition to the photodetector, each pixel has an active amplifier. CMOS sensors are active pixel sensors build over CMOS technology. The CMOS sensor structure is also pixel based, the difference to the CCD being that each pixel in the CMOS sensor is made of a combined set of two or three N-MOSFET and P-MOSFET and the fact that, being an active sensor, the amplifier electronics are at pixel level unlike the CCD where the charges are transfer. Figure 1.7 shows the pixel structure of a CMOS sensor that implements a Bayer filter as a color separation mechanism [28].

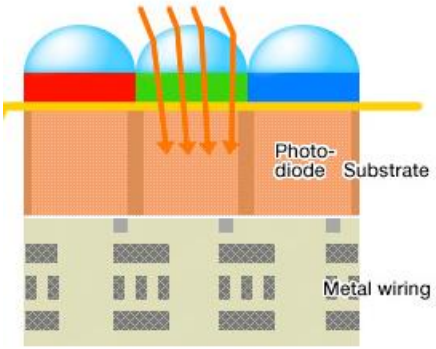

Figure 1.7: Pixel structure of a CMOS sensor that implements a Bayer filter as a color separation mechanism. The difference to the CCD being that each pixel in the CMOS sensor is made of a combined set of two or three N-MOSFET and P-MOSFET and the fact that, being an active sensor, the amplifier electronics are at pixel level unlike the CCD where the charges are transfer [28].

This differences in the sensor's structure implies a different process of capture. Figure 1.8 presents the schematic of the process followed by the CMOS sensor to capture and image. The main difference to the schematic of Figure 1.6 (CCD capture) is that the read out of each pixel is done independently at pixel level.

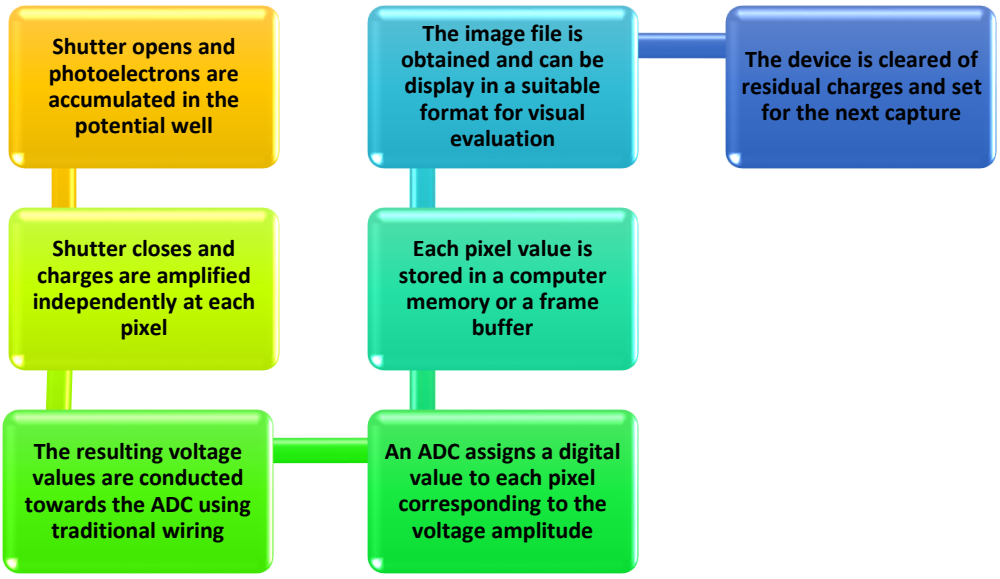

Figure 1.8: Schematic of the process followed by the CMOS sensor to capture and image. The main difference to the schematic of Figure 1.5 (CCD capture) is that the read out of each pixel is done independently at pixel level.

1.3.3 CCD and CMOS Tradeoff

The main difference between CCD and CMOS sensors is the cost of the device. CMOS sensor use techniques and technologies much alike those used in the construction of microprocessors. By amplifying the charges at each pixel the instant result is an analog signal that can be treated by traditional electronic techniques. On the other hand, CCD sensors must implement sophisticated manufacturing processes to be able to transport the charges without distortion and read them at the electronic stage of the sensor. The difference in cost comes mainly from this principles of operation.

On the one hand, for the CMOS to have the electronic amplification so close to the photodetector, it increases significantly the levels of electronic noise that will eventually distort the measured intensity values. On the other hand, this compactness implies a reduction in size of the sensor in comparison to a CCD (with the same photosensitive area) and also due to the lack of the sophisticated electronics present in the CCD, the effective power consumption of CMOS is also lower than that of a CCD.

Another drawback of CMOS sensors is that since each of their pixels are formed by multiple transistors, there's more of a chance of incident photons reaching the transistor instead of the photodiode, which in turn results in an overall lower sensitivity. CCD however, can obtain very high quality images.

Finally, CCD sensors have been mass produced for a longer period of time since they were the leading technology in the digital imaging field; in this sense they represent a more mature technology and thus there are devices in the market that yield higher quality images and have a

higher amount of pixels than CMOS sensor. However as CMOS technology matures and the quality of its devices becomes competitive to CCD sensors, future changes are continuously expected in image sensor technologies [29]–[33].

1.3.4 High Dynamic Range Imaging

Some applications of the Image Sensor System, including fluorescence measurements, result in a significant increase in image quality if a high dynamic rang (HDR) capture is done as opposed to a low dynamic range (LDR). An HDR capture becomes needed for capturing images that have both very low and very high intensity values (large dynamic range). HDR captures can be obtain by many methods; some by physical mechanisms and others by software implementations [34].

Over the years, multiple algorithms have been developed that are able to render HDR images. Among them, the most notable and widely used include Mann and Picard quantification scheme [35], the Mitsunga and Nayar SNR model [36], the variance models of Robertson [37] and Kirk and Andersen [38] and the hat function developed by Debevec and Malik [39]. In this thesis we will pay specific attention to the latter, which is an algorithm capable of capturing both very low and very high intensities by focusing on medium intensity values and at the same time capturing data in the extreme exposure conditions. Every HDR algorithm is based on a weighting function. Said function plays the role of adjusting the pixel intensity value by assigning a weight which will make it possible to render a visible final image. Equation 1.3 shows the weighting function for the Debevec and Malik algorithm. In general, the irradiance of a given pixel is obtained by the expression in equation 1.4 [40].

$$w(v) = min[v_i - v_{min}; v_{MAX} - v_i] \tag{1.3}$$

$$\mu_x = \frac{\sum_i w(v_i) * \frac{g(v_i)}{t_i}}{\sum_i w(v_i)} \tag{1.4}$$

Where,

‘μ_x’ is the average intensity.

‘w (v)’ is the weighting function referred to before.

‘g (v)’ is the inverse of the camera’s function response.

‘t’ is the exposure time.

‘v’ is the non-averaged intensity.

‘i’ is the capture sub-index.

1.4 Lens Free Microscopy

Light microscopy has been an irreplaceable tool in life sciences for several centuries. The quest to resolve smaller features with better resolution and contrast has improved its capabilities at the expense of relatively increasing its size and complexity [41]. A push towards new optical microscopy modalities has risen in the past decade in order to provide complementary solutions to market needs. Along this line an alternative lens free imaging platform has been recently developed combining high resolution and large FOV. In this modality, digital in-line holograms of micro-objects are recorded on a sensor array using partially coherent illumination such that the entire area of the sensor serves as the imaging FOV. To overcome the limits posed by the pixel size of the sensor, superresolution is applied to achieve micron lateral resolution without compromising the FOV [42].

Figure 1.9 shows the schematic and prototype of the lens free microscope (LFM) used for the samples captured in the laboratory. (a) Is the schematic of the LFM, comprising the light source S, the sample volume SV and the image sensor IS. (b) Shows the prototype used; above in the XY mount an optical fiber is placed, which is coupled to an RGB light source. (c) shows the CMOS image sensor within the prototype casing; it is a 5MP sensor of XY dimensions 5.7mmX4.28mm, thus achieving a >24mm^2 FOV.

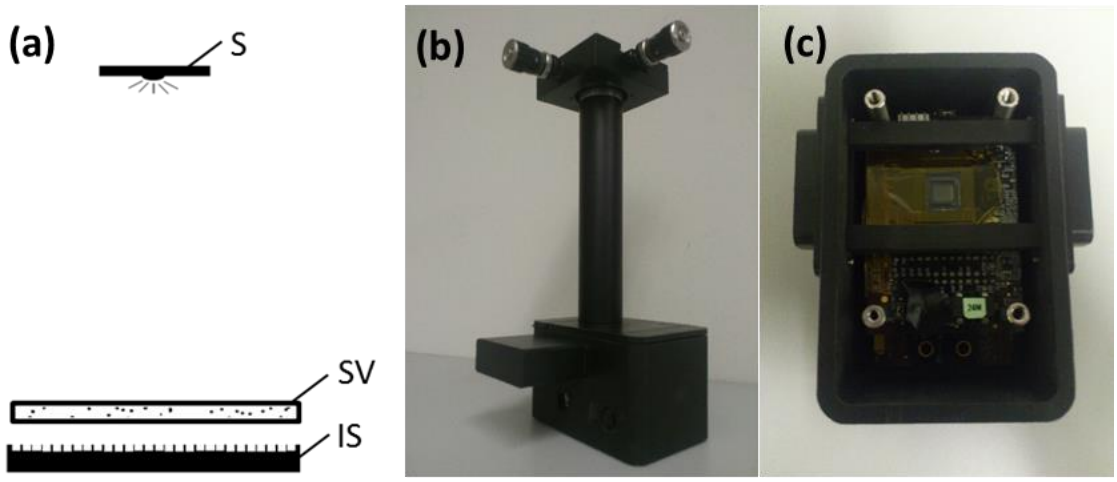

Figure 1.9: Schematic and prototype of the LFM used for the samples captured in the laboratory. (a) Is the schematic of the LFM, comprising the light source S, the sample volume SV and the image sensor IS. (b) Shows the prototype used; above in the XY mount an optical fiber is placed, which is coupled to an RGB light source. (c) shows the CMOS image sensor within the prototype casing; it is a 5MP sensor of XY dimensions 5.7mmX4.28mm, thus achieving a >24mm^2 FOV.

1.4.1 Compressive Sampling

To further improve the performance of the LFM prototype, compressive sampling techniques can be applied along with those of superresolution. Compressive sampling is a novel sampling paradigm that goes against the common wisdom in data acquisition (Shannon's theorem). Compressive sampling theory asserts that one can recover certain signals and images from far fewer samples and measurements than traditional methods use; provided said signal is of sparse or compressible nature. Sparsity expresses the idea that the information rate of a continuous signal

might be much smaller than suggested by its bandwidth [43]. Mathematically speaking (see equation 1.5), there is a vector *(x)* and a sampling matrix *(ϕ)* which is a concise representation of the vector *(x)* in a proper orthonormal basis. Sampling the original vector with the orthonormal basis will result in a vector *(y).*

$$y = \Phi \cdot x \tag{1.5}$$

Note that the sparse nature of vector *(x)* implies that its representation *(ϕ)* has few non-zero elements; therefore the sampled signal *(y)* is also composed mostly by null elements. For the recovery of the signal, a solution to equation 1.6 must be found. Due the potentially large size of matrix *(ϕ)* and its high content of null elements, inverting said matrix would imply a high computational cost for which numerical methods such as l1 minimization.

$$\Phi^{-1} \cdot y = x \tag{1.6}$$

In LFM the use of compressive sampling can partially undo the effects of diffraction, which is an inherent result of lens free operation. To this end, a signal *(x)* is modeled as a point source, a valid orthonormal representation of said signal could be the response of the imaging system to such input signal; this is known as a point spread function (PSF). In turn the sampled version of signal *(x)* will be the diffracted capture *(y).* Based on this, for any arbitrary distribution of point sources at object plane, to which the micrometric particulate to analyze can be approximated, is possible to calculate the expected captured pattern at sensor plane. Therefore using an appropriate numerical method the system induced diffraction can be partially accounted for and counteracted.

1.5 Fluorescence Microscopy

The absorption and subsequent re-radiation of light by organic and inorganic specimens is typically the result of a well-established and well known physical phenomena described as being either fluorescence or phosphorescence. The emission of light through the fluorescence process is nearly simultaneous, with a delay from emission to excitation ranging below the microsecond barrier. On the other hand when the emission persist long after excitation has been extinguished, the process is defined as phosphorescence [44].

The technique of fluorescence microscopy has become an essential tool in the biomedical sciences. The use of an array of fluorochromes makes it possible to identify cells and sub-microscopic cellular components with a high degree of specificity; in fact the technique allows to reveal the presence of a single molecule [45]. In addition, the use of multiple probes (multiple fluorochromes) helps to simultaneously identify several target molecules [46].

Principle of Operation

Fluorescence microscopy is based on exciting a sample stained with a determined fluorochrome or a set of them and detecting its emission or lack of by capturing the sample with an image sensor or viewing the results on real-time through an observation tube or through a screen if the device permits it [47]. Each fluorochrome has a determined excitation bandwidth and peak, just as it has an emission bandwidth and peak. Figure 1.10 shows the spectrum for the excitation and emission of the green fluorescence protein (GFP). In the same sense, for the biomedical applications, certain

pathogens or cells can be bounded to a fluorochrome and through examining the sample with a fluorescence microscope a diagnosis can be made in terms of the emission and its intensity [48].

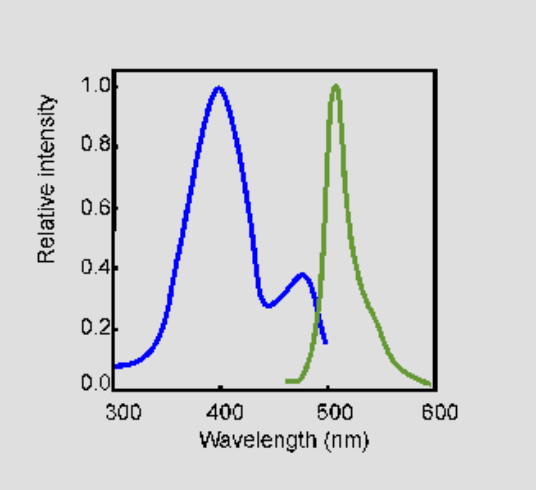

Figure 1.10: The excitation spectrum of native GFP has two excitation maxima at 395 nm and at 470 nm. The fluorescence emission spectrum (green) has a peak at 509 nm and a shoulder at 540 nm [49].

The intensity emitted by a fluorescent probe follows the form in equation 1.5:

$$I = I_0 * K * \varphi * (1 - \mathrm{e}^{-\varepsilon * c * l}) \tag{1.5}$$

However, with the exception of very low values of intensity, the previous equation follows a linear approximation [48]:

$$I = I_0 * K * \varphi * \varepsilon * c * l \tag{1.6}$$

Where,

I_0 is the pump (excitation) power [W].

K is the system's capturing constant defined mainly by the numerical aperture of the sensor and the attenuation of the fluorescence filter.

φ is the sample's Quantum Yield. #photons emitted/#photons absorbed

ε is the Molar Absorptivity [$M^{-1}cm^{-1}$].

c is the concentration of the fluorescence dye [mol/m^3] = [M].

l is the length of the cell or sample [cm].

Dimensional Analysis:

$$[W]=[W]*[\ M^{-1}cm^{-1}]*[M]*[cm] \tag{1.7}$$

Re-radiation Phenomena

Certain conditions come into play within the fluorescence detection techniques that ultimately affect the emission of the sample; this means it eventually reduces or cancels the intensity of the emission. The general term for this phenomena is fading; a catch-all category that is subsequently classified into photo bleaching and quenching. Photo bleaching is the total decomposition of the fluorescent molecules in their excited stage and it is a result of the interaction of the molecules with molecular oxygen. Figure 5 displays the effect of photo bleaching through a series of digital images taken at different time points. The sample is a multiply-stained animal tissue cell sample. The nuclei was stained to emit blue fluorescence, the mitochondria red fluorescence and the actin cytoskeleton green fluorescence. Captures were taken at two minute intervals and the setup was prepared to excite the three fluorochromes in the sample simultaneously. Figure 1.11 (a) through (c) show how the blue fluorescence of the nuclei fades at a much higher rate than the green and red fluorescence; however all three of them drop significantly over 10 minutes [44], [50].

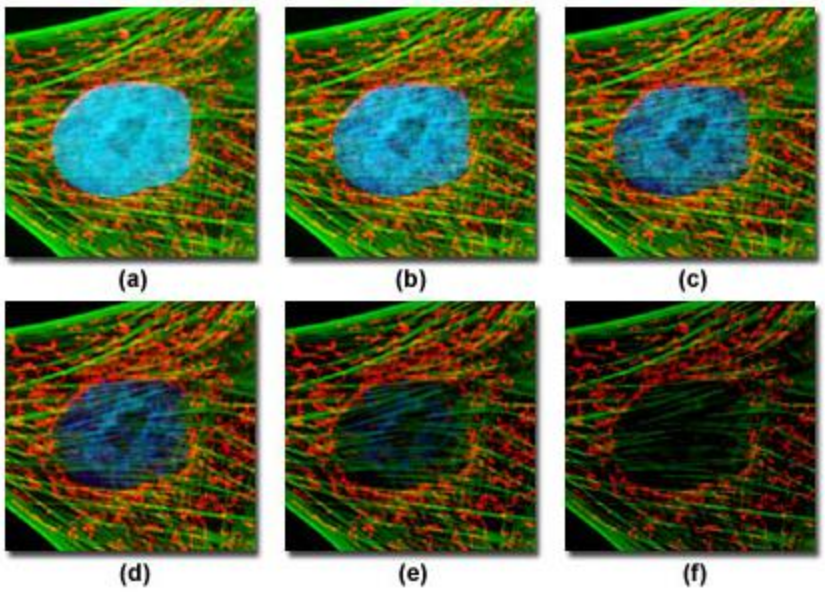

Figure 1.11: Effect of photo bleaching through a series of digital images taken at different time points. The sample is a multiply-stained animal tissue cell sample. Captures were taken at two minute intervals and the setup was prepared to excite the three fluorochromes in the sample simultaneously. Figure 5 (a) through (c) show how the blue fluorescence of the nuclei fades at a much higher rate than the green and red fluorescence; however all three of them drop significantly over 10 minutes [44].

Quenching is the fading through a variety of non-radiative energy losses; it frequently occurs due to oxidizing agents or the presence of salts, heavy metals or halogens compounds. In some other case, quenching can result from the transfer of energy to another nearby molecule (termed acceptor) which is physically close to the excited fluorochromes (termed donor); the acceptor is by nature excited by the donor and thus the resulting fluorescent emission is at the wavelength emitted by the acceptor [51]. This process is known as Fluorescent Resonance Energy Transfer (FRET) and it has recently become the focus of studies involving molecular interaction. Figure 1.12 represents the FRET phenomena: through intermolecular association, the process can be induced; the result is green fluorescence emission while exciting at the emission wavelength of the Blue Fluorescence Protein (BFP) [44], [48].

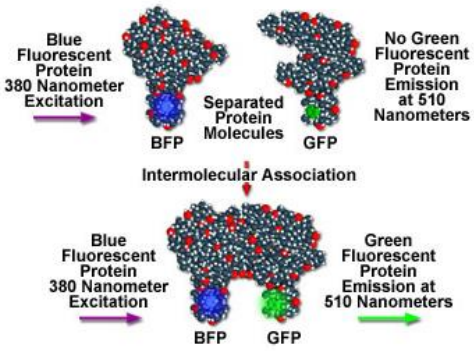

Figure 1.12: representation of the FRET phenomena through intermolecular association, the process can be induced; the result is green fluorescence emission while exciting at the emission wavelength of the Blue Fluorescence Protein (BFP) [44].

1.5.1 Fluorescent Microscope Novel Techniques

In recent years, many new technologies and devices in the field of fluorescent microscopy have been developed with the intention of putting on the market high quality products of reduced cost and multiple features. Traditional fluorescent microscopes are complex devices as the one shown in Figure 1.13. The figure displays a cutaway diagram of an Epi-fluorescent microscope. The system is that of a simple reflected light microscope in which the wavelength of the reflected light is longer than that of the excitation. The excitation light passes through a wavelength selective filter, then it goes through the microscope objective to excite the sample. Once the sample emits fluorescence, it goes through a filter that rejects unwanted excitation wavelengths and then the sample can either be captured by the CCD or seen through the observation tubes [44].

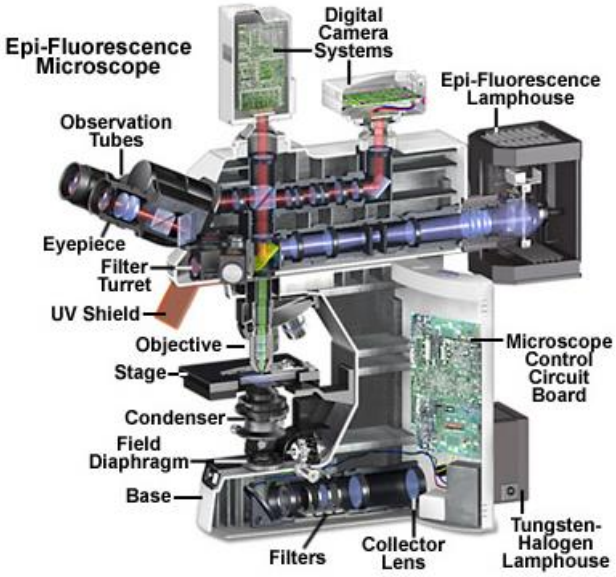

Figure 1.13: Cutaway diagram of an Epi-fluorescent microscope. The system is that of a simple reflected light microscope in which the wavelength of the reflected light is longer than that of the excitation. The excitation light passes through a wavelength selective, then it goes through the microscope objective to excite the sample. Once the sample emits

fluorescence, it goes through a filter that rejects unwanted excitation wavelengths and then the sample can either be captured by the CCD or seen through the observation tubes [44].

In any case the device of Figure 1.13 is not only complex but bulky and expensive. Current trends on fluorescent microscopy are leading to a more compact low-cost solution capable of achieving similar results. Multiple research groups have been making significant efforts towards a fluorescent microscope system for point of care applications, the following systems served as reference points for the development of the prototype designed and tested within the scope of the present work.

UCLA (Aydogan Ozcan)

The department of Electrical Engineering along with the California NanoSystems Institute, have published two different systems of a fluorescent microscope having each a different geometry. The first one is a 3D printed attachment to a mobile phone's camera, with a FOV 80mm^2 together with spatial resolution of 20µm. In addition, if compressive sampling techniques are applied the system can achieve 5µm resolution. The compressive sampling implementation means the deconvolution of the recovered image with the system's Point Spread Function (PSF). To obtain said PSF they use isolated microspheres of 4µm and 10µm. Figures 1.14 and 1.15 show both of the implementations for their mobile phone attachment [5], [12], [13].

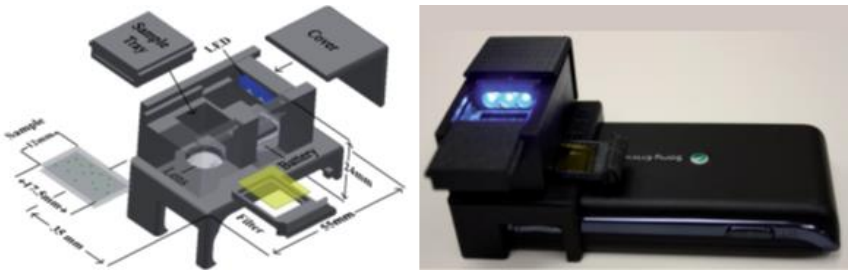

Figure 1.14: attachment build for a Sony smartphone, the fluorescent pump consists of blue LEDs placed perpendicular to the detection path, a plastic color filter is used to eliminate the remaining pump and improve the dark field condition and the pump is guided within the sample cuvette to uniformly excite the specimen. To focus the fluorescence emission a simple external lens is placed just above the mobile's internal lens rendering possible the imaging of the sample particles [13].

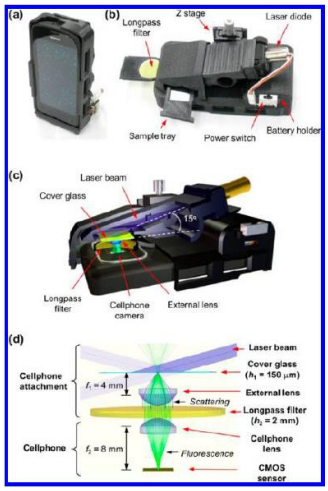

Figure 1.15: implementation of the system in a Nokia Siemens mobile phone, the main difference with the previous system is the use of an inclined pump at 75 rather than 90º. A similar filter is placed between the external and internal lenses and in this case the pump source is a blue laser diode [5].

Figure 1.14 represents an attachment built for a Sony smartphone, the fluorescent pump consists of blue LEDs placed perpendicularly to the detection path, a plastic color filter is used to eliminate the remaining pump and improve the dark field condition and the pump is guided within the sample cuvette to uniformly excite the specimen. To focus the fluorescence emission a simple external lens is placed just above the mobile's internal lens rendering possible the imaging of the sample particles. Figure 1.15 shows the implementation the system for a Nokia Siemens mobile phone, the main difference with the previous system is the use of an inclined pump at 75 rather than 90º. A similar filter is placed between the external and internal lenses and in this case the pump source is a blue laser diode.

Figure 1.16 shows the results obtained with the prototype of Figure 1.14; images from a conventional fluorescent microscope with a 10x objective are also shown for comparison. Figures A-1 through C-1 were decoded using compressing sampling techniques achieve results (A-2 through C-2) similar in resolution to the conventional microscope. The white arrows show a slight shift in the particles position and orientation due to the solution the particle is suspended on.

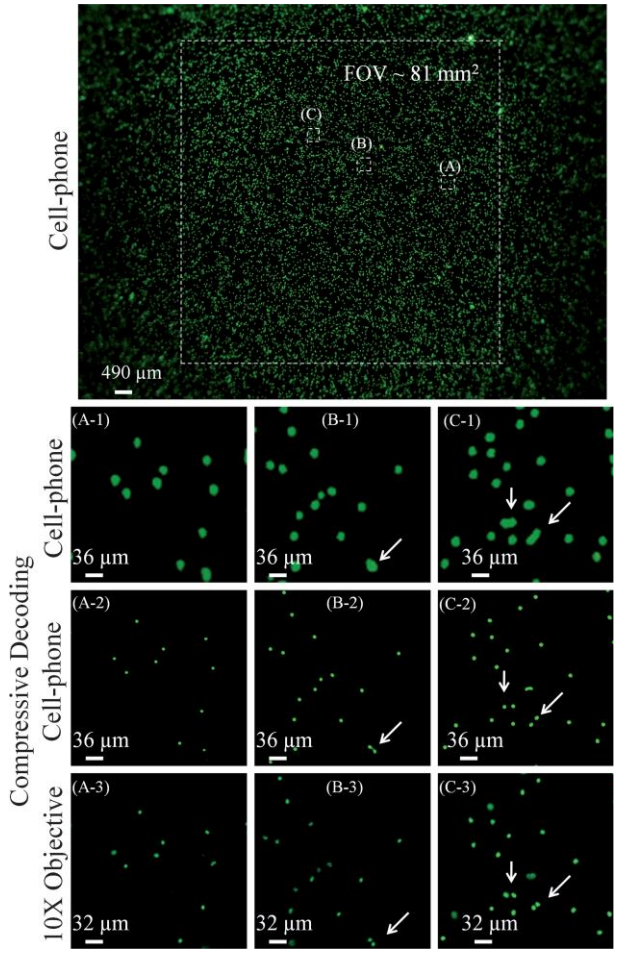

Figure 1.16: results obtained with the prototype of Figure 1.14; images from a conventional fluorescent microscope with a 10x objective are also shown for comparison. Figures A-1 through C-1 were decoded using compressing sampling techniques achieve results (A-2 through C-2) similar in resolution to the conventional microscope. The white arrows show a slight shift in the particles position and orientation due to the solution the particle is suspended on. The images are pseudo-colored in green [13].

The second system published by Aydogan Ozcan's group at UCLA is a lens free implementation of a fluorescence microscope. Figure 1.17 shows the schematic, experimental setup and results of their earlier lens free platform, in which a FOV of about 80mm^2 is achieved with a spatial resolution of 10µm. A prism is used to remove the pump by the principle of Total Internal Reflection (TIR). After the sample an absorption filter with thickness <100µm is placed and then the CCD/CMOS device for imaging. Two experimental setups are shown KAF-8300 (Figures B and C) and KAF-39000 (Figures D and E); their difference is the pixel size of the CCD employed (5.4µm and 6.4µm respectively) [10], [11].

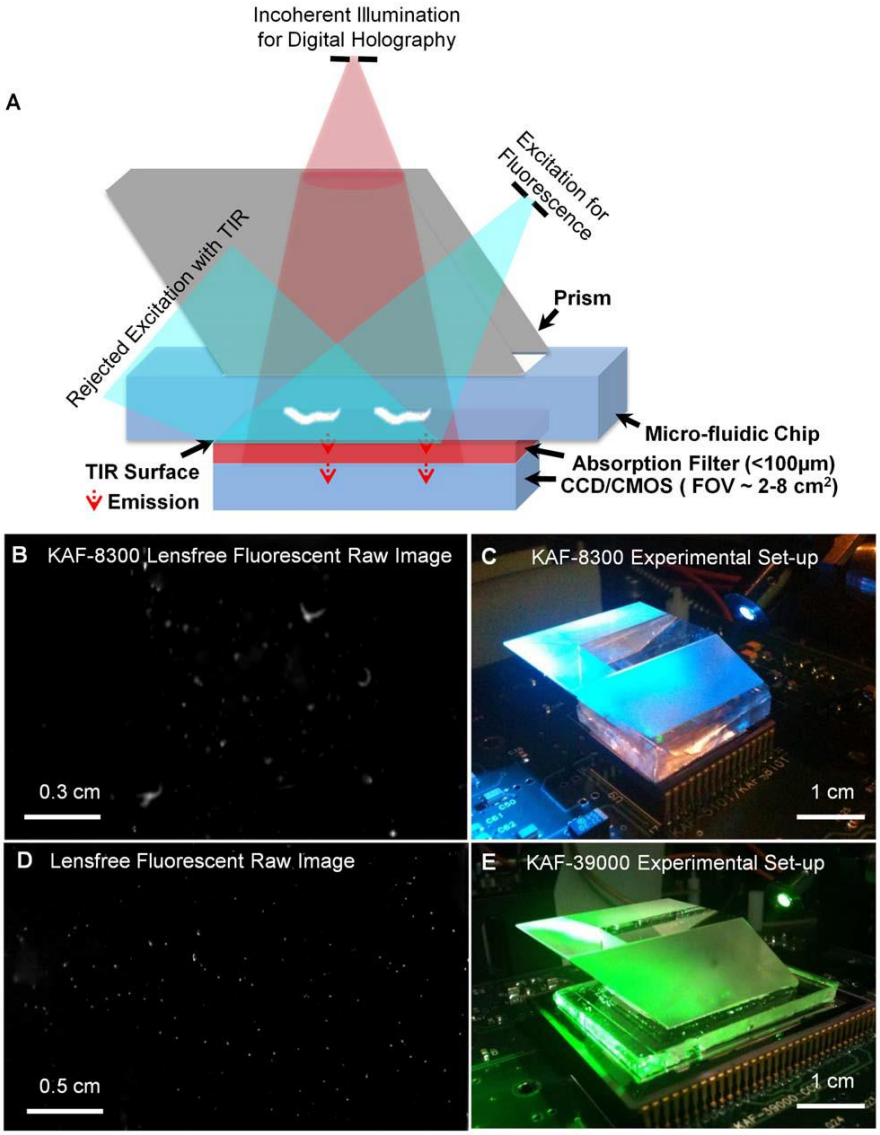

Figure 1.17: schematic, experimental setup and results of their earlier lens free platform, in which a FOV of about 80mm² is achieved with a spatial resolution of 10μm. A prism is used to remove the pump by the principle of Total Internal Reflection (TIR). The following the sample an absorption filter with thickness <100μm is placed and then the CCD/CMOS device for imaging. Two experimental setups are shown KAF-8300 (Figures B and C) and KAF-39000 (Figures D and E); their difference is the pixel size of the CCD employed (5.4μm and 6.4μm respectively) [10].

The second lens free implementation is based under the same principle with the addition of a fiber optic face-plate tapered such that the density of the fiber optic wave-guides on the top facet is >5 times larger than the bottom one; in combination of a compressive sampling algorithm, a spatial resolution of <4μm is obtained over a FOV of approximately 60mm². Figure 1.18 shows the experimental setup, the schematic and microscopic views of the top and bottom facet of the fiber face-plate. Figure 1.19 shows the fluorescence imaging results comparing the recovered image before and after compressive sampling decoding and again with a 10x microscopic image [10], [11].

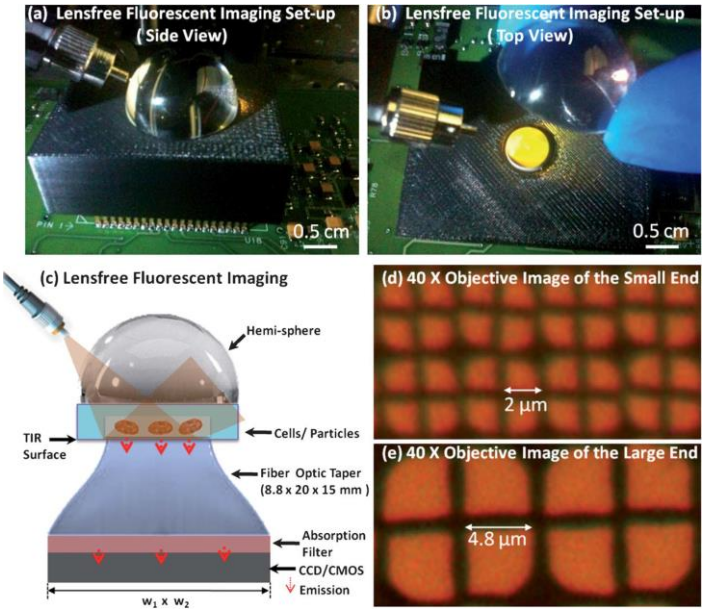

Figure 1.18: experimental setup, the schematic and microscopic views of the top and bottom facet of the fiber face-plate. The use of the fiber optic face-pate combined with a compressive sampling algorithm a spatial resolution of <4µm is obtained over a FOV of approximately 60mm² [10].

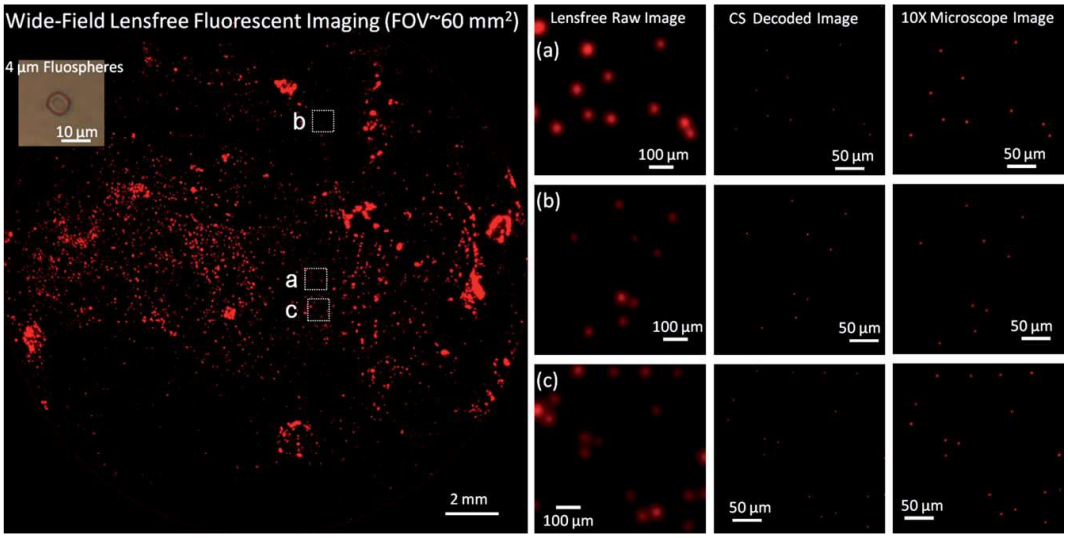

Figure 1.19: the fluorescence imaging results comparing the recovered image before and after compressive sampling decoding and again with a 10x microscopic image. The images are pseudo-colored in red [10].

Figure 1.20 shows the capabilities of the compressive sampling algorithm employed by the UCLA group, as they can resolve overlapping fluorescent emission patterns arising from the particles. The inset decoded images illustrate for comparison purposes bright field microscopic images of the same particles. The lens free images are pseudo-colored in red.

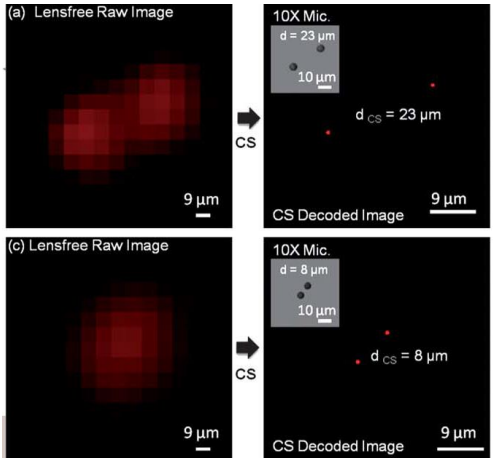

Figure 1.20: representation of the capabilities of the compressive sampling algorithm employed by the UCLA group, as they can resolve overlapping fluorescent emission patterns arising from the particles. The inset decoded images illustrate for comparison purposes bright field microscopic images of the same particles. The lens free images are pseudo-colored in red [10].

Caltech (Silo-Filter CMOS)

The department of Electrical Engineering at Caltech along with the center for bio analysis from the Korea Research Institute of Standards and Science, developed a chip-scale fluorescent microscope by designing an image sensor with metal walls between neighboring pixels bounding an absorptive filter; the principle is to guide the fluorescence emission with the metal walls through the filter down to the sensor's photodiode. The result is a fluorescent LFM that can also be used for bright field captures. Figure 1.21 displays the schematic of the chip-scale microscope (a), a micrograph of the metal grid structure (b) and a schematic diagram of the Silo-Filter structure. Figure 1.22 shows the results in bright field and fluorescent captures using the designed microscope. The FOV is of 4.8mmx4.4mm with spatial resolution of 13µm [2].

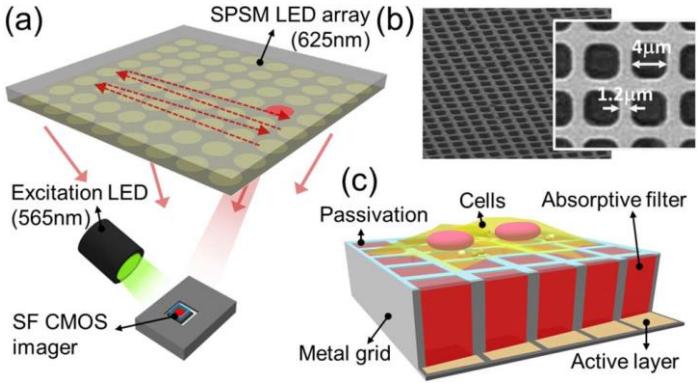

Figure 1.21: displays the schematic of the chip-scale microscope (a), a micrograph of the metal grid structure (b) and a schematic diagram of the Silo-Filter structure [2].

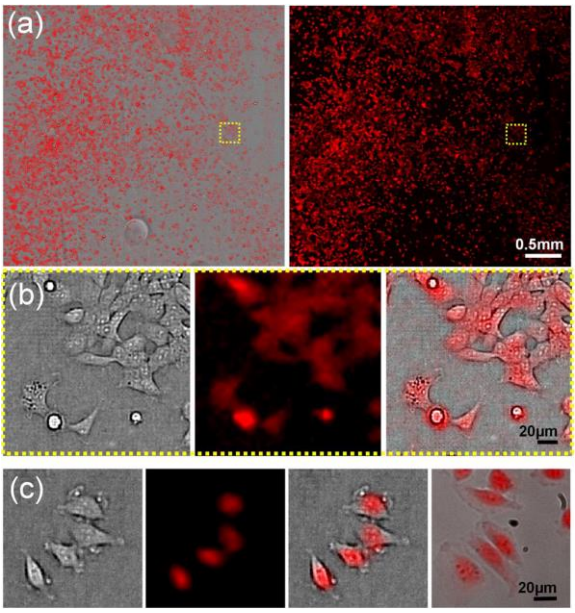

Figure 1.22: results in bright field and fluorescent captures using the microscope developed at Caltech shown in the schematic of Figure 8. The FOV is of 4.8mmx4.4mm with spatial resolution of 13μm [2].

Fraunhofer Institute for Biomedical Engineering

This institute has developed a handheld optical sensor for quantification of fluorescent microarrays. On the surface of a planar waveguide, fluorescently labeled particles are excited by the evanescent field of the guided light and the emitted fluorescence is detected by implanting a system made of a pinhole array followed by a microlens array. Figure 1.23 represents a comprehensive schematic comprehensive view of the principle behind the device. The laser illumination is coupled into the waveguide, the particles are excited by the evanescent filed and as much as possible their emission is guided towards the microlens array through the pinhole array, the lens then focuses the emission that travels down a filter to create the dark field condition and is detected by a CCD image sensor [4].

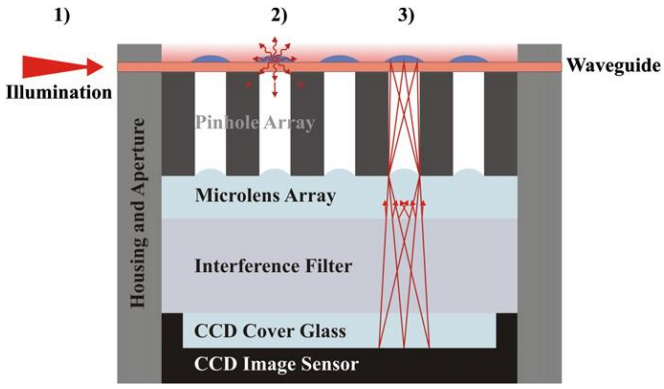

Figure 1.23: Comprehensive schematic comprehensive view of the principle behind the device. The laser illumination is coupled into the waveguide, the particles are excited by the evanescent filed and as much as possible their emission is guided towards the microlens array through the pinhole array, the lens then focuses the emission that travels down a filter to create the dark field condition and is detected by a CCD image sensor [4].

Figure 1.24 compares the results obtained using this novel microarray reader (left) with a reference laser scanner (right). Due to the optical configuration of the microarray reader, some degree of magnification can be observed in the image. Also some blurriness is detected which is due to the imager limitations. Note that this device is not design for imaging purposes but for intensity quantification only.

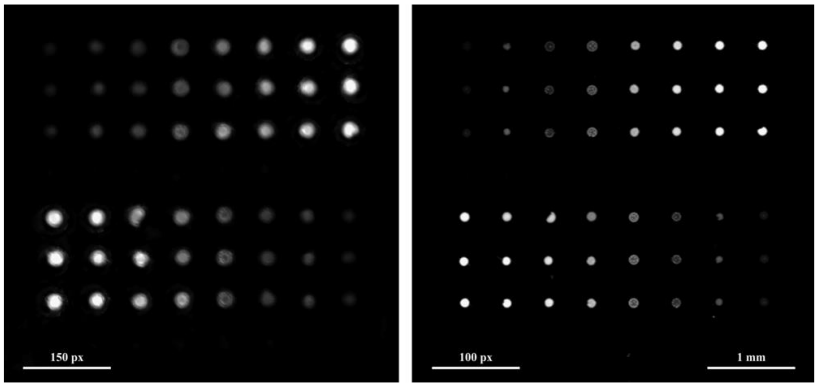

Figure 1.24: comparison of the results obtained using this novel microarray reader (left) with a reference laser scanner (right). Due to the optical configuration of the microarray reader, some degree of magnification can be observed in the image. Also some blurriness is detected which is due to the imager limitations [4].

Stanford

The departments of computer science and biochemistry of Stanford University developed a Light Field Microscope capable of capturing the light fields of biological samples. They achieve this by inserting a microlens array into the optical path of a conventional microscope. To compensate for the diffraction effects they apply a focus stacking imaging technique to recover the sample's light field. Focus stacking is based on taking multiple captures at different focal distances which results on an image with a greater depth of field. Figure 1.25 displays an image of the Light Field Microscope prototype, in which the optomechanics of a conventional microscope are employed, a microlens array is introduced between the sample and the image sensor, in the position marked by the red circle [15]–[17].

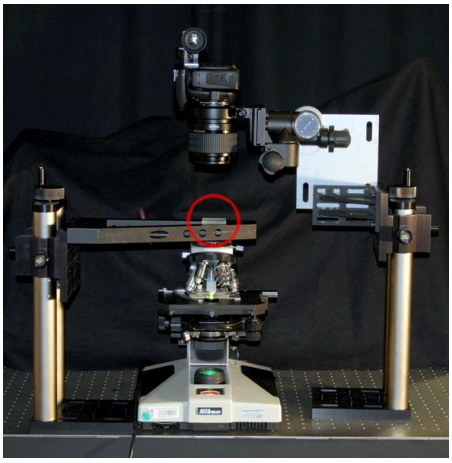

Figure 1.25: image of the Light Field Microscope prototype, in which the optomechanics of a conventional microscope are employed, a microlens array is introduced between the sample and the image sensor, in the position marked by the red circle [15].

Figure 1.26 show a capture of a speck of fluorescent crayon using the prototype of Figure 1.24. To the left the complete FOV is shown with detail on the microlens array. To the right different reconstructions of the captured image are shown. The full image is made out of several sub-images, one for every microlens; each sub-image has 20^2 pixels. By taking one pixel from each sub-image different perspectives of the captured sample can be recovered with that improved depth of field. In the lower right the image represented are obtain by summing the pixels of each sub-image; this results in an orthographic representation of the sample as that of a conventional microscope but with lower spatial resolution.

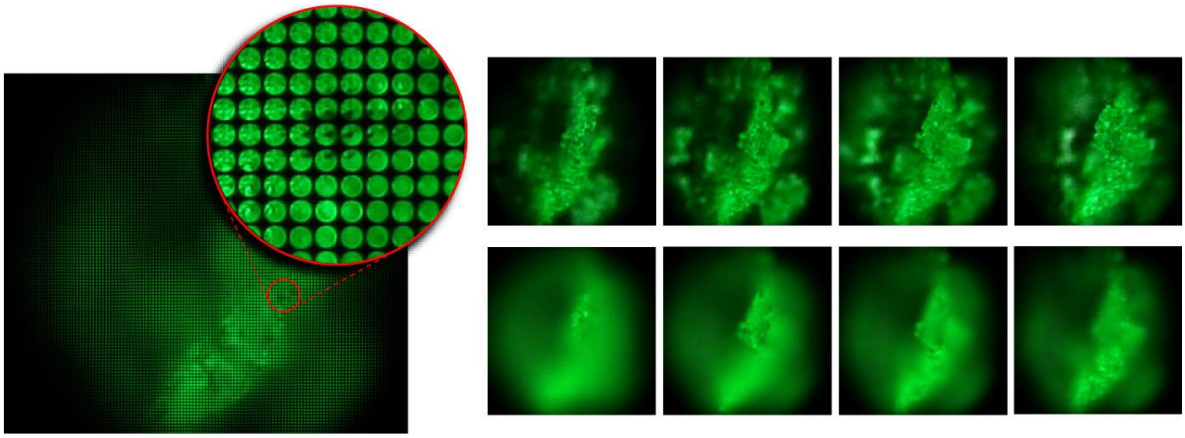

Figure 1.26: capture of a speck of fluorescent crayon using the prototype of Figure 14. To the left the complete FOV is shown with detail on the microlens array. The full image is made out of several sub-images, one for every microlens; each sub-image has 20^2 pixels. By taking one pixel from each sub-image different perspectives (top right) of the captured sample can be recovered with that improved depth of field. In the lower right the image represented are obtain by summing the pixels of each sub-image; this results in an orthographic representation of the sample as that of a conventional microscope but with lower spatial resolution [15].

1.6 Volumetric Analysis in Image Cytometers based on Fourier Optics Principles

A converging lens inherently performs two-dimensional Fourier transform. The information to be Fourier-transformed is introduced into the optical system by a sample with amplitude that is proportional to the input function of interest.

Let a volumetric sample be placed immediately in front of a converging lens of focal length f_{length}. The input is assumed to be uniformly illuminated by a normally incident wave. After the lens the field distribution is proportional to the two-dimensional Fourier transform of that portion of the field subtended by the lens aperture. The complex amplitude distribution of the field in the focal plane of the lens is the Fraunhofer diffraction pattern of the field incident on the lens, even though the distance to the observation plane is equal to the focal length of the lens. The amplitude and phase of the light field are determined by the amplitude and phase of the input Fourier components at frequencies ($f_{spatial}=u/(\lambda*f_{length})$); said frequencies are dependent on the spatial distribution of the wave front (u) the emission wavelength (λ) and the focal length of the converging lens (f_{length}). The Fourier transform relation between the input amplitude transmittance and the focal-plane amplitude distribution is not a complete one, due to the presence of the quadratic phase factor that precedes the integral. While the phase distribution across the focal plane is not the same as the phase distribution across the spectrum of the input, the difference between the two is a simple phase curvature. In the case of the proposed design, it is the intensity across the focal plane that is

of real interest, for which this phase curvature can be dismissed. This phase term is important if the ultimate goal is to calculate another field distribution after further propagation, in which case the complete complex field is needed. In this case, however, the intensity distribution in the focal plane will be taken, and the phase distribution is of no consequence. Measurement of the intensity distribution yields knowledge of the power spectrum (or more accurately, the energy spectrum) of the input, and from this spectrum it is possible to retrieve information linked to the nature of the specimen. The detection of the specimen's spatial Fourier transform with an image sensor device as used in image cytometry techniques would allow for the processing and analysis of this information known to be linked to the specimen under study [52]. Fourier transforms can be inverted, the Fourier transform of a diffraction pattern will reveal the structure of the object [53], [54].

Consider next a more specific geometry. The input volume sample, located a distance d in front of the lens, is illuminated by a normally incident wave. When the sample is placed in the front focal plane of the lens, the phase curvature disappears, leaving an exact Fourier transform relation. In practice, when the Fourier transform of the sample is of prime interest, it is often preferred to place the input directly against the lens in order to minimize vignetting, although in analysis it is generally convenient to place the input in the front focal plane, where the transform relation is unencumbered with quadratic phase factors.

For a 2-dimensional signal as would be the sample volume, the pattern retrieved that corresponds to the spatial Fourier transform follows the expression of equation 1.5.

$$I_{(x,y)} \approx \left[\frac{A}{2\lambda Z_i}\right]^2 \cdot sinc^2\left(\frac{2wy}{\lambda Z_i}\right)\left\{sinc^2\left(\frac{2wx}{\lambda Z_i}\right) + \frac{m^2}{4} sinc^2\left[\frac{2w}{\lambda Z_i}(x + f_0 \lambda Z_i)\right] + \frac{m^2}{4} sinc^2\left[\frac{2w}{\lambda Z_i}(x - f_0 \lambda Z_i)\right]\right\} \quad (1.4)$$

For most image cytometry applications such as those within the food industry and water analysis a high volumetric sample must be measured to comply with regulations; for instance, volumes of up to 1l must be tested for the microorganism population control in water analysis. Using laboratory techniques a liter of water can be concentrated down to a volume between 1ml and 5ml; therefore the market requires a system that can measure a few milliliters of sample volume. Parting from these requirements, this work focuses on the creation of an optical cytometer capable of measuring samples with a wide FOV and a large DOF, which in turn signifies the measure of a high volumetric sample (few milliliters) within a single capture.

The principle behind the system is the far-field detection and analysis of a spatial Fourier transform of the specimen's wave front by means of an array of light sensors. Said array digitizes the data for processing; the captured data contains information on both amplitude and phase of the sample's transform (the complex Fourier transform). This provides the functionalization of an optical cytometer that performs sample analysis on the frequency domain; this results on an increase on the analyzed volume and an improvement in terms of reliability of said data. The system analyzes the particulates in terms of complexity and size as well as concentration (counting).

The concept is the design of the system and apparatus capable of doing the aforementioned analysis. A lens system is mounted in the path between the sample volume and the array of light sensors; said lens system takes advantage of the principles behind Fourier optics to recover the spatial Fourier transform of the specimen's wave front.

1.7 Aim of the Thesis

In this project we aim for a low cost, low energy consumption, portable optical cytometer using advanced CMOS detection. This will allow such technology to move out of the lab and find widespread point-of-care applications, achieving a portable device, especially suitable for remote areas. The objective is to design and test an opto-mechanical device and its corresponding software platform, capable of rapidly analyzing sample volumes with a large field of view and depth of field. To validate the resulting technology the system is tested with real biological samples from a wide range of fields. Applications on tuberculosis, pneumonia, water microorganisms, toxicity and cell viability will be mainly explored using the novel optical cytometer. The final objective is to complete the construction of a validated pre-industrial device.

1.8 Outline of the Thesis

The rest of this thesis is organized as follows. Chapter 2 focuses on the development and modifications to the software platform that constitutes the optical cytometer; it discloses the main algorithms developed and proves their performance with the results from a broad variety of samples captured. Chapter 3 describes the structure and operation of the optical cytometer designed within the scope of this work and displays the most significant results through which the validation of the apparatus was consolidated. Finally chapter 4 draws conclusions from the work presented in this thesis and proposes future lines of work to both improve the designed device and increase its functionalities for the different application fields.

2 Imaging System

This chapter summarizes the most significant achievements on the development of the software platform that controls the image cytometer. The sample information is captured by the optical cytometer using a capturing algorithm developed in C++. Once the sample image has been captured, a set of corrections over the captured signal is performed as well as specific processing depending on the targeted sensing application; this post-processing is done on Python. Within the scope of this work, the main efforts were on the consolidation of a solid capturing algorithm. An optimization of the low dynamic range (LDR) capture was performed and a high dynamic range (HDR) algorithm was developed. The performance of the algorithms developed is tested by capturing a wide variety of samples.

2.1 Exposure Time and Gain Optimization for LDR captures

In order to obtain reliable images from the sensor without necessarily knowing which exposure time is ideal for a certain sample, is imperative that to optimize this parameter before capturing. This is relevant for low dynamic range (LDR) captures since in high dynamic range (HDR) captures there is no single optimum exposure time so an averaging of multiple captures is needed (a particular algorithm was programmed for HDR captures, which is explained in the following section).

In an LDR, there may be cases of low intensity or high intensity depending on the sample, cytometer and source lighting. However in terms of image processing, the goal is to obtain a reliable image but yet recognizable, by the human eye, regardless of the aforementioned variables.

Having this in mind an optimization of the exposure time was design to return an expected average power, input from the handling interface. In this sense the sample would be captured using a suitable exposure time to result, as it was already mentioned, in a reliable and recognizable image.

An optimization algorithm was designed and programmed, based on an adapted proportional integral derivative (PID) logic. A PID algorithm optimizes a given parameter based on three factors (Proportional, Integral and Derivative). The proportional factor, produces a value that is proportional to the current error; the integral factor is proportional to the cumulative error in time and finally the derivative is proportional to the variation of such error.

For the Image sensing system, an adaptation of a classic PID controller was programmed, reducing to a minimum the computational cost without risking the quality of the results. The applied algorithm takes an average value from the handling interface and before moving on to the LDR capture, optimizes the exposure time based on the current error and its variation (compared to the previous error). This optimization is done per channel (pixel color); at the end the maximum value is kept and the gain optimization algorithm is run.

The interest, as exposed in the exposure time optimization, is to move our input signal to a given average power set as an ADC level; in this sense, the modifications to the pixel gain should take place before converting it into the digital domain, thus only the analog gain is to be modified. Some

tuning could also be achieved by changing the analog offset however that was not the approach taken.

It is important to understand the values taken by the actual total gain when a certain input string is written in the camera's registers. And the Datasheet of the sensor implemented was found to have a lack of reliable information on the matter. So before programming the routine some work was done on testing and understanding the values written on the gain registers. The results are summarized in the following table. In conclusion, it was seen that the analog gain register could also be used to attenuate the signal for some register values.

Analog Gain Register	Total Gain	Increments
1-63	0.125-7.875	0.125

Table 2.1: Analog Gain Register values along with the corresponding Total Gain values and the increment ratio

Having understood this information about the analog and digital processes that the sensor performs, it is now possible to go through the details of the programmed optimization. Firstly, let it be explained why the time taken form the exposure optimization was the highest.

Before any optimization is performed, the gains per channel are maximized with the analog gain part of the register to the maximum to our effects (Total Gain: 7.875). This maximization allows a broader input range to the ADC which results in better intensity resolution. Having in mind that low light scenes require a high exposure time, it can be concluded that after time optimization the highest resulting value will be that of the channel with the lowest light intensity (remember that at this point all gains are equal and maximum). Given this scenario, by lowering the gain on the remaining channels, it is possible to adapt the light intensity of these channels to the optimized exposure time. In essence, this is how the algorithm works. In case the time algorithm did not converged the gain optimization will be attempted to all four channels. If at the end of both algorithms, convergence is still not achieved, specific recommendations are given to the user on how to resolve the issue.

In detail, the algorithm attempts optimization by obtaining the difference between the expected and the computed average power; if such difference is negative, the gain is reduced while, on the contrary, it is increased. The variation step is the minimum allowed by the changes in the analog gain section of sensor's register (0.125). It does so, keeping in mind the maximum value allowed (7.875).

2.2 HDR Capturing Algorithm

For the exposure time limits a script was programmed that resulted in a minimum and maximum exposure time. The user can choose whether the sweep is linear or exponential. The minimum exposure time will be the minimum time corresponding to which a given setting of pixels are not sub-saturated. The maximum will be the minimum time corresponding to which all pixels are not sub-saturated. Sub-saturation is defined as the pixel intensity just below the dark noise level.

A multiple capture approach was selected, this means many captures are taken for different exposure times and then they are averaged by a known weighting function; for the developed algorithm Debevec and Malik's hat weighting function was employed [39]. The algorithm

implements the corresponding equations (1.3 and 1.4) for the multiple captures of each channel obtaining a resulting average. In detail, the processes followed by the algorithm are synthetized as follows:

- Calculates the exposure time excursion.
- For each channel:
    - Sets the step according to the number of exposures type of excursion.
    - For each exposure:
        - Sets the current exposure time.
        - For each capture (the user can performed multiple captures per exposure time):
            - ✓ It calculates iteratively and for each pixel the numerator and denominator on equation 1.4.
    - It calculates for each pixel the irradiance according to equation 1.4.

A matrix is return containing the normalized pixel intensity values. The algorithm starts with the longest exposure time and it performs under a logic such that if a pixel is correctly captured for a given exposure time (no saturation on any of the iterative captures), then said pixel is no longer captured in the following exposures. This allows a faster and more efficient performance of the algorithm.

2.3 Capturing Algorithm Results and Discussion

Multiple samples were captured to test the strength of the developed algorithms. Bear in mind the objective is to be able to efficiently capture samples with both very high and low intensity values and to be capable of recognizing shapes and structures within said sample by avoiding the saturation or sub-saturation of any pixel in the CMOS. The first approach was to take photographs with the sensor using a barrel lens to traditionally recover the image of a scene. In order to prove the strength of the algorithms the scene captured was view of the laboratory in low light conditions with a high intensity desk lamp placed as to cover lower right corner of the CMOS FOV. Although they are not of a particular setup, they are sufficient prove that the capturing algorithms have improved and that such improvements can be replicated when tested in specific imaging prototypes.

Figure 2.1 displays the capture in the laboratory on low light conditions with the high intensity desk lamp at a section of the FOV. (a) Shows an LDR capture with a deliberate exposure time of 1ms; the result is an image generally low in brightness in which neither the low intensity nor the high intensity sections of the photograph can be clearly distinguish. (b) Shows the same capture in LDR after optimizing the exposure time to 2.77ms and gains per channel using the PID logic within the developed algorithm; this time the low light sections of the photograph, which take most of the FOV, are efficiently imaged with every detail of the scene being clearly identify. However the very high intensity section saturates the pixels on the CMOS resulting on loss of information in the photograph. Finally (c) displays the HDR capture of the same scene, by properly sweeping the exposure time and averaging these captures it is possible to efficiently capture both low and high intensity sections in a single image.

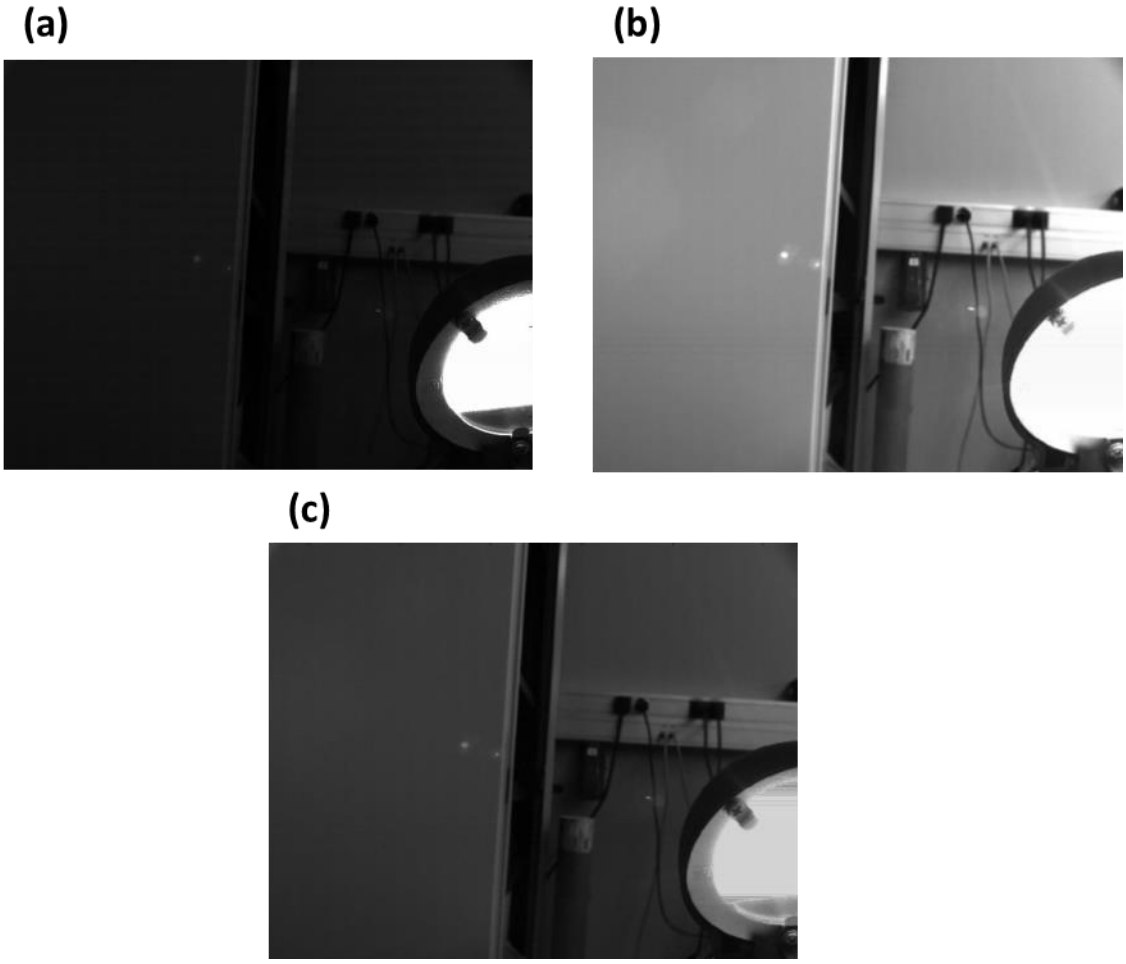

Figure 2.1: Captures in the laboratory on low light conditions with the high intensity desk lamp at a section of the FOV. (a) Shows an LDR capture with a deliberate exposure time; the result is an image generally low in brightness in which neither the low intensity nor the high intensity sections of the photograph can be clearly distinguish. (b) Shows the same capture in LDR after optimizing the exposure time and gain using the PID logic within the developed algorithm; this time the low light sections of the photograph, which take most of the FOV, are efficiently imaged with every detail of the scene being clearly identify. However the very high intensity section saturates the pixels on the CMOS resulting on loss of information in the photograph. Finally (c) displays the HDR capture of the same scene, by properly sweeping the exposure time and averaging these captures it is possible to efficiently capture both low and high intensity sections in a single image.

To test the capabilities of the algorithms developed in more appropriate conditions in terms of target applications, a set of captures was taken of micrometric structures and real biological samples using the LFM prototype of Figure 1.9. Figure 2.2 shows an optimized LDR captured in both exposure time and gain for a green channel of the CMOS sensor. (a) Displays the image of the captured structure with the LFM prototype of Figure 1.9; (b) displays the histogram of said image. Note how the general shape of the structure can be distinguished as well as the different sub-structures within the sample. However high saturation of the signal persists; which is an inherent consequence of LDR captures regardless of the time optimization. The algorithm uses PID logic to fix a time and gain values to optimally capture the pixels at mean intensity within the incident wave front; as a consequence, pixel values that are highly distanced from said mean will saturate or sub-saturate the sensor.

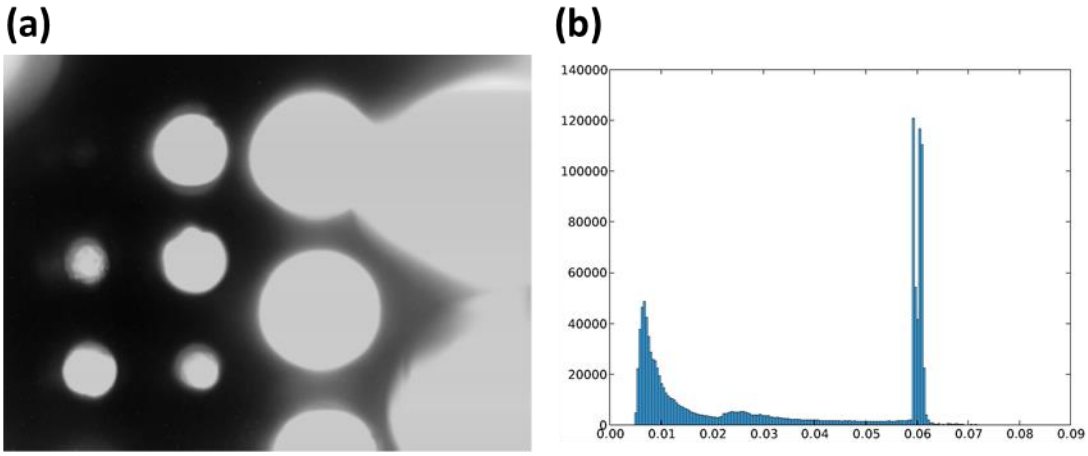

Figure 2.2: Optimized LDR captured in both exposure time and gain for a green channel of the CMOS sensor. (a) Displays the image of the captured structure with the LFM prototype of Figure 1.9; (b) displays the histogram of said image. Note how the general shape of the structure can be distinguished as well as the different sub-structures within the sample. However high saturation of the signal persists; which is an inherent consequence of LDR captures regardless of the time optimization.

To resolve the inconvenience posed by the previous example, an HDR algorithm was developed and implemented. With the appropriate weighting function it is possible to perform a sweep in exposure times, as explained in section 2.2. Figure 2.3 shows the digital representation of the structure capture; it is a sparse mask (a binary matrix) with 77% sparsity (zero values). The computer generated structure was sent for fabrication with dimensions such that the outcome sample will be slightly bigger than the CMOS surface and thus possible to cover the complete FOV. Figure 2.4 displays a green channel capture of said structure for both LDR and HDR operation. (a) is the LDR image, (b) the histogram of the LDR image; from them a large amount of saturated pixels can be noted (over $700x10^3$ pixels). (c) is the HDR image and (d) its corresponding histogram; from them it can be noted that no saturation or sub-saturation of the pixels is present and in the image details on the structure's shape are now visible.

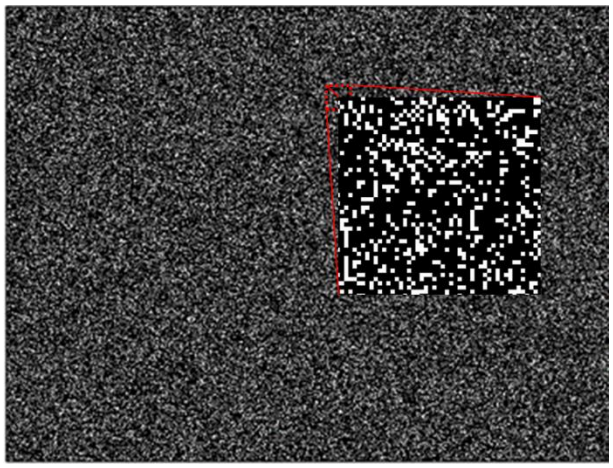

Figure 2.3: Computer generated representation of the structure capture; it is a sparse mask (a binary matrix) with 77% Sparsity (zero values). The digitally designed structure was sent for fabrication with dimensions such that the outcome sample will be slightly bigger than the CMOS surface and thus possible to cover the complete FOV.

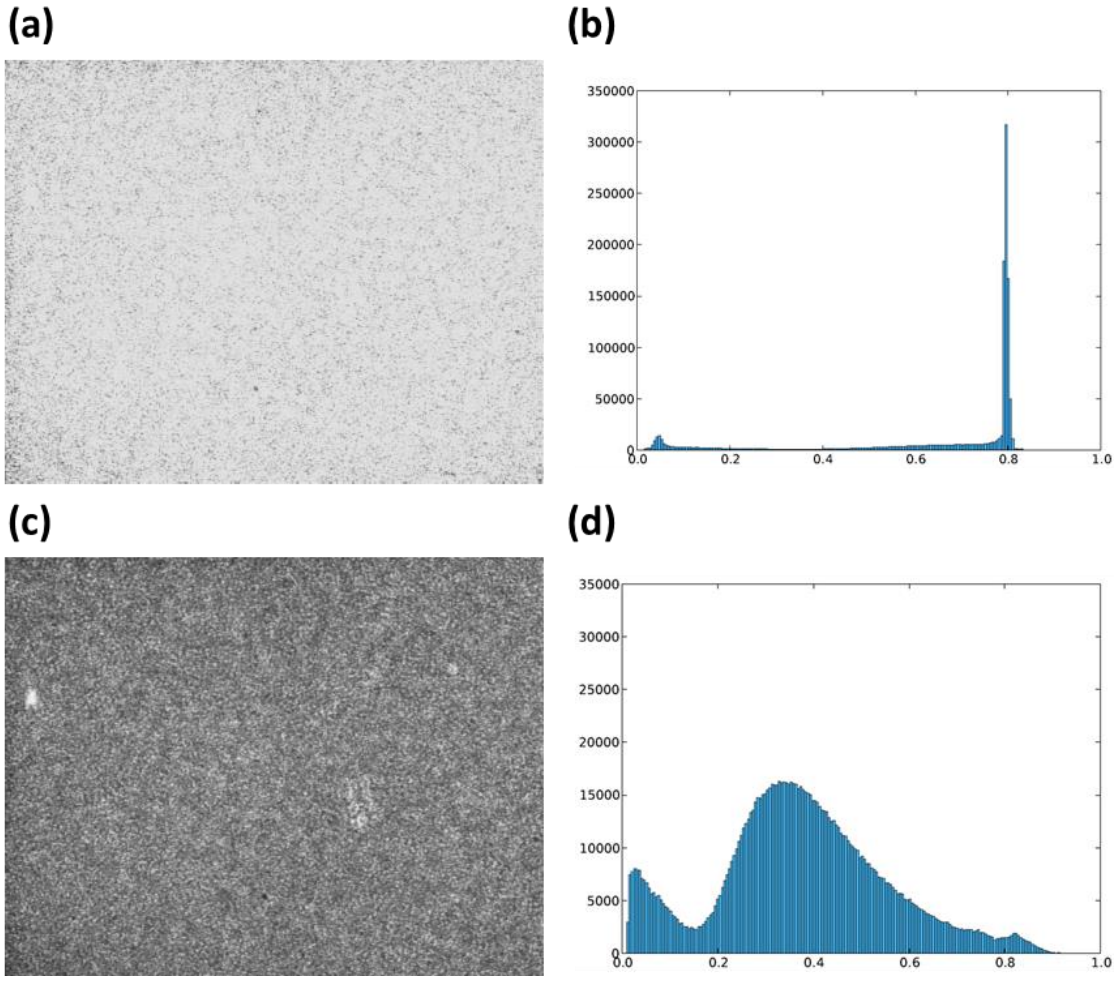

Figure 2.4: Green channel capture of a sparse physical matrix for both LDR and HDR operation. (a) is the LDR image, (b) the histogram of the LDR image; from them a large amount of saturated pixels can be noted (over 700x10^3 pixels). (c) is the HDR image and (d) its corresponding histogram; from them it can be noted that no saturation or sub-saturation of the pixels is present and in the image details on the structure's shape are now visible.

The structures chosen to prove the strength of the system were of extreme circumstances, in which near zero intensity values coexist in the frame with very high intensity values. The following stage was to test the imaging system with real biological samples.

2.4 Imaging System Results and Discussion

Figure 1.9 shows the experimental lens free microscope setup in which sample volumes of Jurkat cells and E. coli microorganisms were measured. A LFM is an image microscope composed by a light source and an image sensor; the sample is placed in the light path between the source and the sensor and finally a diffracted image of the sample is captured with the algorithm described in chapter 2. Initially, a set of samples was captured with a LFM to test its imaging capabilities and to evaluate what change would be needed to achieve a system complying with the applications of interest.

With the prototype of Figure 1.9 two main objectives were accomplished. First, the imaging capabilities of the designed capturing algorithm, in both HDR and LDR for real biological samples. Second, the viability of using the LFM as a cytometer that retrieves an image of the sample and allows for concentrations estimate. These goals were validated by capturing and characterizing a variety of sample volumes such as the ones contained in this report. A pattern composed of cubic sub-structures of Titania (Titanium Dioxide) of dimensions 50x50x50µm^3, a particle slide of 5µm probes, Jurkat cells and Escherichia coli (E. coli) in several concentrations. Jurkat cells are an immortalized line of human T-lymphocyte with a size of about 15µm, E. coli is a rod shape anaerobic bacterium with a length of about 2µm.

Titania Pattern and Particle Slide Characterization

These samples were captured to demonstrate the capability of the system of detecting, distinguishing and identifying micrometric bodies. The Titania pattern can be detected thanks to the reflective nature of the material. Figure 2.5 shows a section (200x200µm^2 approx.) of the recovered image of the pattern where the multiple sub-structures can be clearly identified. The particle slide represents a more random distribution of particulate within a sample; being in turn closer to a real biological sample. Figure 2.6 shows the recovered image of the particle slide in which once again the micrometric probes within the slide are clearly distinguished. The capture was achieved over the complete FOV of the CMOS sensor (>24mm^2) with a recovered pixel size of 1.1µm.

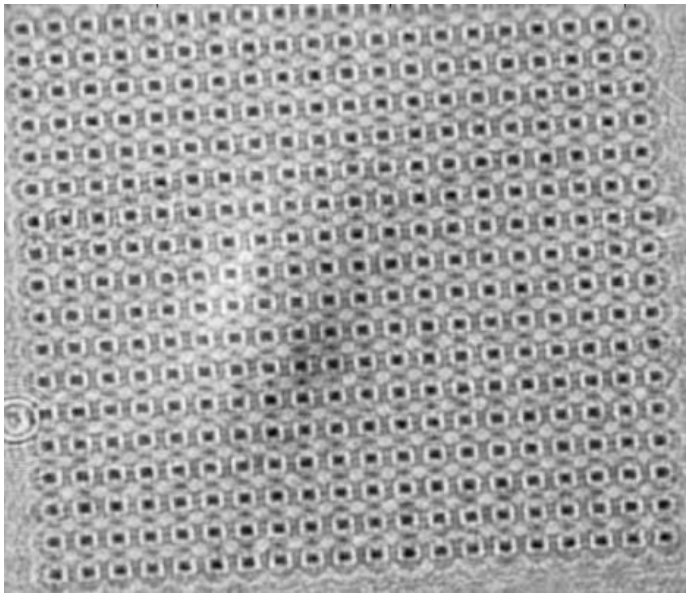

Figure 2.5: A pattern composed of cubic sub-structures of Titania (Titanium Dioxide) of dimensions 50x50x50µm3. Section (4mm^2 approx.) of the recovered image of the pattern were the multiple sub-structures can be clearly identified. The imaging is possible due to the reflection of the Titania with respect to the Silica (Silicon Oxide) substrate.

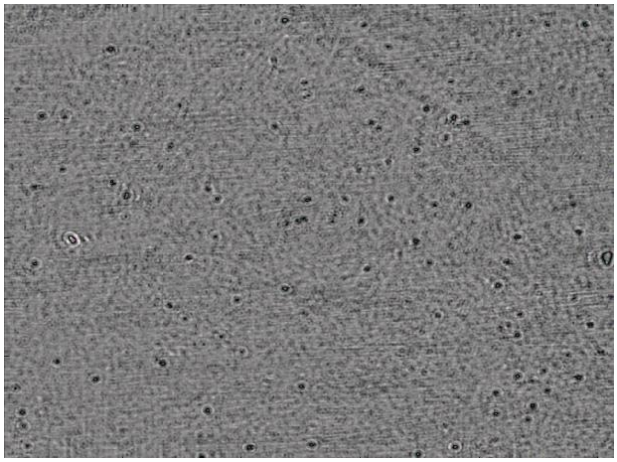

Figure 2.6: recovered image of the particle slide in which once again the micrometric probes within the slide are clearly distinguished. The captured slide contains equal size probes of 5µm. The capture was achieved for the complete FOV of the CMOS sensor (>24mm²) with a recovered pixel size of 1.1µm.

Jurkat Cells Characterization

Three different concentrations of Jurkat cells were prepared and captured; each concentration was delivered in a cylindrical container labeled as (Tube 1, 2 and 3). All three concentrations of the samples were prepared and mounted on several slides for examination under the LFM prototype. A 5µl volume of the sample was mounted on a microscope slide chamber, this was repeated twice for each of the original concentrations obtaining a total of six samples to be tested (two of each).

Each sample was captured separately in all three colors (RGB – two captures of green), taking advantage of the Bayer filter configuration of the CMOS image sensor in use. Also for each capture a measure of the camera's Dark Noise and Reference illumination was taken in order to apply the first corrections to the captured image, thus removing the defects inherently introduced by the system. In all initial capture of the samples, the cells were distorted due mainly to the diffraction suffered from the plane of incidence of the light on the sample to the image sensor plane; the image recovery algorithm fights these unwanted effects.

The following step is to recover the image at the sample plane, thus removing the effects and distortions introduced by diffraction and to apply techniques of super resolution microscopy that allows the improvement of the spatial resolution in the resulting image; also by using a compressive sampling algorithm is possible to further improve quality by recovering the system's response (point spread function - PSF) and using it for image corrections. On the resulting image there's a pixel size of 1.1µm. The recovered sample is a color image made up from the four captures obtained, corrected and processed to improve resolution. Figure 2.7 shows the outcome of the recovery algorithm for the three samples of different concentration labeled Tube 1, 2 and 3 corresponding to (a), (b) and (c) respectively. Figure 2.7 (c) is the recovered image with the most disturbances, this is due to deficiencies on sample preparation which damaged the sample. Even though unfortunate, this allows one reflection which is that the series of digital corrections and normalizations applied to the image only removes the defects introduced by the system (such as noise and reference levels) but leaves the sample itself untouched; this means that for a proper mounting of the sample, all information is recovered and most of the system's defects are suppressed.

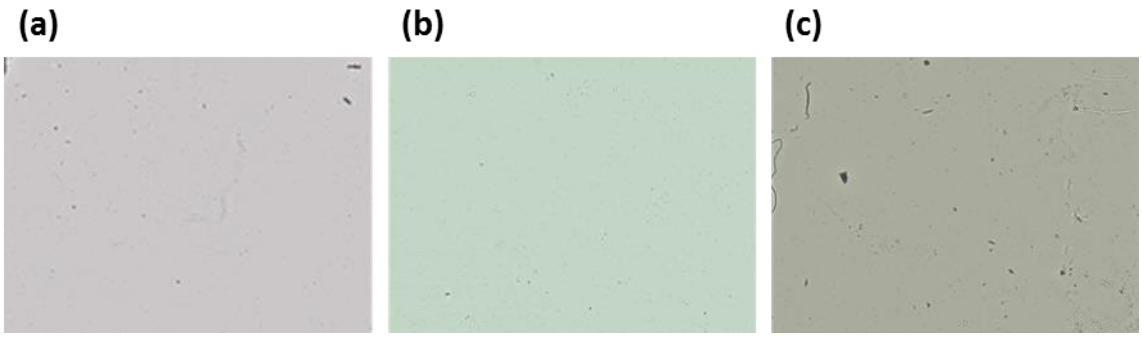

Figure 2.7: Outcome of the recovery algorithm for the three samples of different concentration of Jurkat cells labeled Tube 1, 2 and 3 corresponding to (a), (b) and (c) respectively. Figure 2.4 (c) is the recovered image with the most disturbances, this is due to deficiencies on sample preparation which damaged the sample. In all three images is possible to identify the contained particulate which allows for the estimation of the sample concentration.

The counting of the cells is a main factor of interest for biomedical applications. With the LFM platform, the process of cell counting can be achieved with more reliable statistics from a single capture given the attained FOV of >24mm^2. By examining the recovered samples, the concentrations for samples labeled Tube 1, 2 and 3 were estimated and the record of such can be seen in Table 2.2.

Sample Label	Estimated Concentration (cells/ml)	Calibrated Concentration (cells/ml)
Tube 1	1.02x10^6	0.98x10^6
Tube 2	1.43x10^6	1.5x10^6
Tube 3	2.39x10^6	2.26x10^6

Table 2.2: Concentration estimates of the captured Jurkat cells samples labeled tube 1, 2 and 3. Said concentration were obtained by processing the data in Figures 2.4, 2.5 and 2.6 with a particulate counting algorithm. The calibrated concentration was provided with the samples and it corresponds to data retrieved from a flow cytometer.

Escherichia coli Characterization

After the characterization of the prototype with the Jurkat cells, certain improvements could be applied by optimizing the recovery algorithm. After applying the corresponding changes to the algorithm platform, the prototype was tested again, this time capturing samples of E. coli. As said before, E. coli is a facultative anaerobic bacterium commonly found in the lower intestine of warm-blooded organisms. Due to its ease of manipulation it plays an important role in biological engineering and it is thus an ideal microorganism for testing the developed prototype. Figure 2.8 shows the recovered image of an E. coli sample captured in bright field with the LFM prototype. A FOV of 4.32mmx3.24mm is shown with an image having a pixel size of 1.1µm.

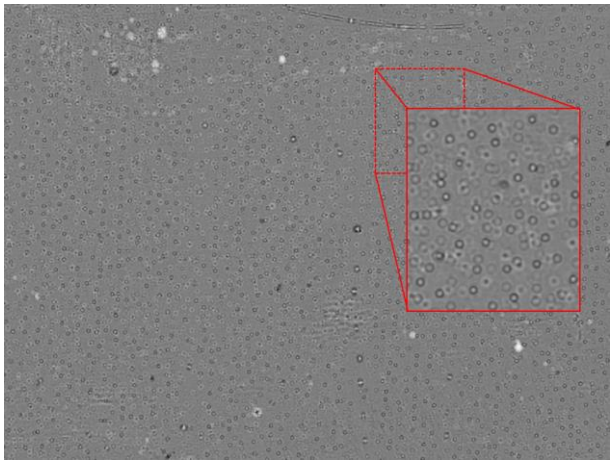

Figure 2.8: Recovered image of an E. coli sample captured in bright field with the LFM prototype. The recovered image is obtained by combining the normalized captures of each individual color channel (Green 1, Red, Blue and Green 2). The normalization of the captures consists on removing the CMOS dark noise and accounting for the reference intensity input in the system by the light source. In it a FOV of 4.32mmx3.24mm is shown with an image having a pixel size of 1.1µm. The highlighted region represents a zoom in the marked area.

Figure 2.9 shows the same sample of Figure 2.8 after processing it through the compressive sampling algorithm. An improvement on the identification of the particulate is achieved as some diffraction effects are counteracted. The outer rings remaining on the image are resulting artifacts from the reconstruction known as twin image. There's a magnification on the capture of about 3X which allows the proper detection with the setup of a bacterium with an average size of 2µm. The highlighted region represents a zoom in the marked area. It permits a closer identification of the microorganisms obtained from the same capture that retrieves the full FOV.

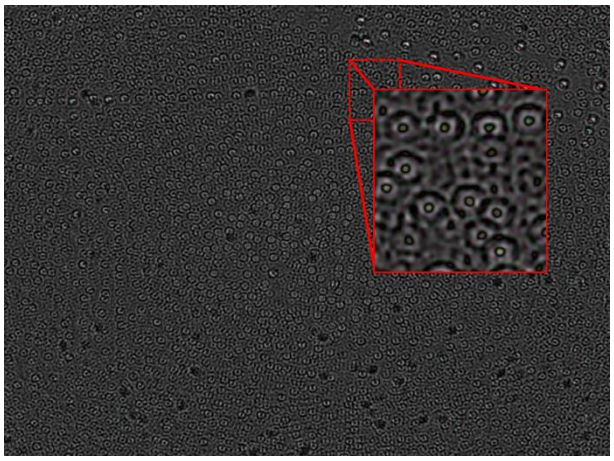

Figure 2.9: Sample of Figure 2.8 after processing it through the compressive sampling algorithm. An improvement on the identification of the particulate is achieved as some diffraction effects are counteracted. The outer rings remaining on the image are resulting artifacts form the reconstruction known as twin image. There's a magnification on the capture of about 3X which allows the proper detection with the setup of a bacterium with an average size of 2µm. The highlighted region represents a zoom in the marked area.

It has been proven that with the LFM prototype, particulates can be imaged and counted. However there's a lack of specificity on the captured particulate which is a requirement for several applications. An approach to gain specificity on the captured samples is to develop a fluorescent

detection scheme. With the interest of improving the features of the designed microscope in terms of FOV, DOF and sensitivity, we had considered a potential modification of the processing optics. The idea is to construct an apparatus capable of measuring small particulate (few micrometers) in low concentrations (as low as 1 particulate per milliliter). There is market desire to maximize the FOV and DOF in the volume sample, therefore improving the sensitivity of the device. To this end, a new design was proposed, which makes use of Fourier optics.

2.5 Summary

A description of the developed algorithms was presented. This included a specific code that was developed to optimize the exposure time and digital gain of the CMOS image sensor based on PID logic. The developed HDR capturing algorithm was analyzed in detail. Said HDR algorithm is a modified implementation of Debevec & Malik's hat function with optimized exposure times using an adaption of the PID algorithm developed for the case of LDR captures. Both algorithms were tested to evaluate their performance; first with specially selected structures that proved the strength of the algorithms and then with real biological samples that proved its capabilities in market applications.

3 Optical Cytometer for Particulate Analysis in Target Specimen Volumes

The design of the optical cytometer for volumetric samples, based on Fourier optics principles, is presented and validated with real biological samples. The optical cytometer developed in this thesis is proven suitable for applications in disease diagnosis, water and food monitoring; using samples of Jurkat and K562 cells and a variety of microorganisms (E. coli, streptococcus and Bordetella). The apparatus presented is shown to be functional in both fluorescent and non-fluorescent modes over a large range of concentrations (10^7CFU/ml – 10^2CFU/ml).

3.1 Cytometer Design

The sample volume is placed before an optical lens at a distance lower than the focal length. After the lens, at a distance equal to the focal length, the received signal will be equivalent to the complex Fourier transform of the volume. Placing a spatially selective filter, will process the acquired transform; at the CMOS image sensor, a complete image is captured. The acquired signal contains information on the amplitude and phase of the input wave front.

Figure 3.1 shows the schematic and laboratory prototype of the designed optical cytometer. (a) Shows a diagram detailing the designed cytometer used for measuring in bright field. The top optical lens focuses the band limited LED light source onto a 1ml volume sample containing the target specimen; the resulting wave front is collected by the processing optics of the system. The image sensor is a CMOS detector. (b) Points out the modification on the previous setting for the measures of fluorescently marked samples, using a fluorescent filter to suppress the pump light. The excited sample generates a fluorescent wave front which is collected by the processing optics. (c) Shows an image of the prototype built in the laboratory.

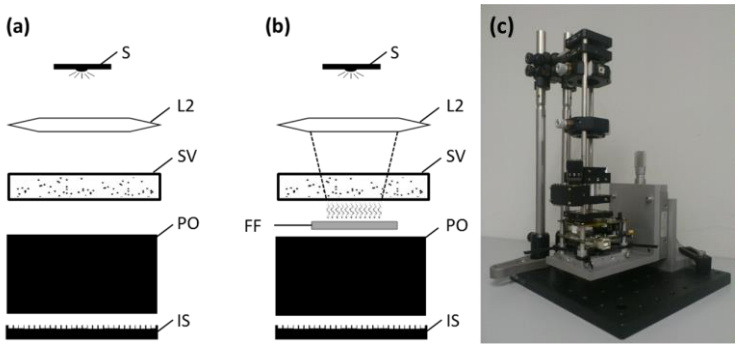

Figure 3.1: Schematic and laboratory prototype of the designed optical cytometer. (a) Diagram detailing the designed cytometer. Comprising a light source (S), an optical lens to focus the light source (L2), the sample volume (SV), a set of processing optics (PO) and a CMOS image sensor (IS). (b) Modification on the previous setting for the experiments with fluorescently marked sample volumes, using an appropriate fluorescent filter (FF) to suppress the remaining pump light. (c) The prototype built in the laboratory.

3.2 Dispersion Graphs and Complexity vs. Size Analysis

The system, as described in the previous section; captures at the sensor level an optically processed signal that is linked to the Fourier transform of the system. As introduced in chapter 1, the detection of the specimen's spatial Fourier transform with an image sensor allows the processing and analysis of this information known to be linked to the specimen under study. As Fourier transforms can be inverted, the Fourier transform of a diffraction pattern will reveal the structure of the object.

From equation 1.4 it is possible to deduct, that a spatial Fourier transform as captured by a detector array will consist on a wave front pattern. Said pattern can be formatted into a periodic set of lobes defined by the bandwidth of the Fourier transform with a given harmonic intensity and lobe area; where the center of the image is the zero spatial frequency and each intense lobe represents a harmonic of the signal captured. Said formatting is achieved by a Fourier descriptor of the captured diffraction pattern; this means a digital fast Fourier transform of the diffracted pattern is applied as the initial step for the statistical analysis of the signal. Figure 3.2 shows the diffracted pattern capture by the system (left) corresponding to the spatial Fourier transform of the sample volume (in this case a particle slide with sizes ranging from 5µm to 16µm) as process by the optics in the device and the formatted Fourier descriptor of the pattern (right) as obtained from the statistical data processing algorithm.

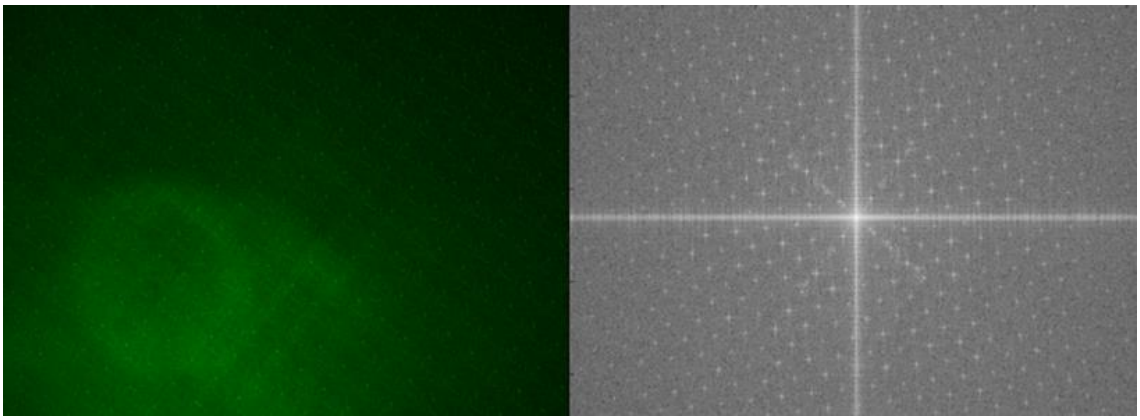

Figure 3.2: diffracted pattern capture by the system (left) corresponding to the spatial Fourier transform of the sample volume (in this case a particle slide with sizes ranging from 5µm to 16µm) as processed by the optics in the device and the formatted Fourier descriptor of the pattern (right) as obtained from the statistical data processing algorithm.

Knowing the details behind the processing optics and the principles behind Fourier theory, two conclusions can be drawn:

- The ratio between the harmonic intensity *($I_{harmonic}$)* and the intensity of the fundamental frequency *($I_{fundamental}$)* is proportional to the complexity of the signal (equation 3.1).
- The area covered by the harmonic's lobe on the image sensor plane *($lobe\ area$)* is inversely proportional to the particle size (equation 3.2).

$$Complexity\ (f_{spatial}) \propto \frac{I_{harmonic}}{I_{fundamental}} \tag{3.1}$$

$$Size\ (f_{spatial}) \propto \frac{\lambda \cdot z}{lobe\ area} \tag{3.2}$$

In this sense, the complexity and size information can be paired into a dispersion graph in which each component represents a given spatial frequency. The complexity and size information extracted from each spatial frequency is in turn related to the particulate contained in the analyzed sample volume. The dispersion graphs obtained by processing the images captured with the optical cytometer presented bear the following technical specifications. Each dot of the graph represents a particular spatial frequency. Particles of the same size may carry different frequency components depending on their complexity. The fundamental harmonic does not yield reliable information on its own; it is a reference for the remaining results. Low frequency components yield high complexity; whereas high frequency components are linked to low complexities.

For the measurement of biological samples the particulate will be suspended on a transparent buffered solution such as a phosphate buffered saline (PBS). Even though such solution has no biological charge on its own other than the target specimen or specimens, the interaction of the light source with the solution will cause effects on the transmitted wave front that may eventually be captured by the sensor. Furthermore, the presence of impurities in the components of the imaging system or the leakage of light reflections external to the system can end up altering the ultimately detected signal. The effects of the buffered solution and the foreign light reflections as well as any other outer intrusion into the optical system constitute the added noise to the captured signal. Therefore when processing the data to retrieve the complexity and size information, measures must be taken to ensure the proper detection of the actual target specimen. These intrusions will induce in the transform harmonics of very low intensity; therefore a threshold is set referred to the intensity of the fundamental frequency below which acquired data will be considered as noise and discarded. The threshold must be adapted depending on the nature of the sample and its radiative effects.

After the noisy data is removed, the resulting complexity and size chart will provide the microbiological charge window, as can be seen in Figures 3.4, 3.5, 3.7 and 3.8. This window refers to the area in the chart linked to the target specimen; it allows for the estimation of concentration based on statistical parameters of the captured signal (pixel intensity sum, mean, standard deviation, maximum and minimum), as shown in Table 3.1.

From the microbiological charge window and the statistical data retrieved, the microbiological charge or total count and the target population are defined and measured. The total count hints to an estimation on the concentration of the target specimen in the volumetric sample; to obtain it, the statistical data inside the detection window is processed. The target population refers to the efficiency of the optical system in detecting the target specimen; it is a ratio between the spatial frequencies considered to be linked to the target specimen and the spatial frequencies consisting of noisy data or non-targeted specimens. These parameters are recorded in Tables 3.3, 3.4 and 3.5.

Having understood the optical system designed and developed the processing algorithms to retrieve the aforementioned data, the optical cytometer of the present thesis was tested with a variety of samples in order to validate its performance within the field.

3.3 E. coli and Mixed Size Particles Characterization

The capabilities of the device are demonstrated by measuring and analyzing different concentrations of E. coli, from 10^8 CFU/ml to 1 CFU/ml both for non-fluorescent sample volumes and for samples marked with the corresponding FITC antibody (Ex. 495 nm/Em. 519 nm).

Concentration Estimates

A series of five E coli samples prepared with concentrations decaying by one order of magnitude between samples. Table 3.1 displays statistics of fluorescence intensity images for samples 1 to 5. The fluorescently marked concentration of E. coli increases from sample 1 to sample 4. While for sample 5 a reduction in intensity level indicates either saturation of fluorescence or erroneous preparation of sample.

Sample label	Sum	Mean	Std.	Max	Min
1	30443	5.43	119.29	26653	1.73e-4
2	60938	1.08	24.42	5479	1.94e-5
3	65501	1.16	26.40	5921	3.75e-5
4	89278	1.59	36.03	8089	7.23e-5
5	84699	1.51	34.88	7843	1.17e-4

Table 3.1: Statistics of fluorescence intensity images for samples 1 to 5. The fluorescently marked concentration of E coli increases from sample 1 to sample 4. While for sample 5 a reduction in intensity level indicates either saturation of fluorescence or erroneous preparation of sample.

Pump Induced Fluorescence Saturation

Fluorescence emission holds a linear relation with the excitation (pump) power. However said relation is dependent on the level of that input pump power and the concentration of the sample. A highly concentrated sample, if excited with a continuous wave at a fixed power, could cause the saturation of the fluorescence emission as the fluorochromes can only emit up to a certain ratio. This rate depends on the energy transitions of the fluorochrome and its quantum yield. In general, a higher quantum yield implies a higher saturation point.

In the current setup, using a square signal with duty cycle 99% and period 1ms, the output optical power of the pump source is about 94mW. In order to avoid saturation, the proposed solution is to use an automatic multi fluorescence pump intensity illumination. This would provide the possibility of capturing the sample with different pump signals that may differ in their duty cycle and LED drive current. At this point an automatism that captures the sample with 5 different duty cycles has been used. The dynamic range of concentration the system is capable of detecting was later proven also with a series of E coli samples of different concentrations.

In Table 3.2 the intensity values for the four different concentration samples over decreasing the fluorescence pump optical intensity are shown. Note that the higher the pump intensity the higher the fluorescence signal and it decreases linearly for low pump intensities. Furthermore, a clear

difference of a factor from 2 to 3 is present between fluorescence intensity signals for increasing CFU concentration samples. Sample 4, 10^7 CFU/ml, presents pump induced saturation for the higher pump intensity level, while the saturation effect is reduced for decreasing pump intensity levels.

Sample label	Pump 100%	Pump 90%	Pump 80%	Pump 70%	Pump 60%	Pump 50%
1 (10^4 CFU/ml)	205105	190286	178345	161149	149570	129830
2 (10^5 CFU/ml)	768471	687016	610359	551536	489627	420893
3 (10^6 CFU/ml)	1248132	1121248	986268	902508	784360	684489
4 (10^7 CFU/ml)	2074353	1832674	1664270	1484522	1290067	1117178

Table 3.2. Intensity values for the 5 different concentration samples over decreasing the fluorescence pump optical intensity. For higher pump intensity the fluorescence signal is higher and it decreases linearly for lower pump intensities. Furthermore, a clear difference of a factor from 2 to 3 is present between fluorescence intensity signals for increasing CFU concentration samples.

Figure 3.3 displays the dynamic range of concentrations detected with the device designed. Different concentrations can be clearly distinguished and identified from 10^8 CFU/ml down to 10^2 CFU/ml (Figure 3.3 (a)). For lower concentrations (10 and 1 UFC/ml) an on and off response can be given.

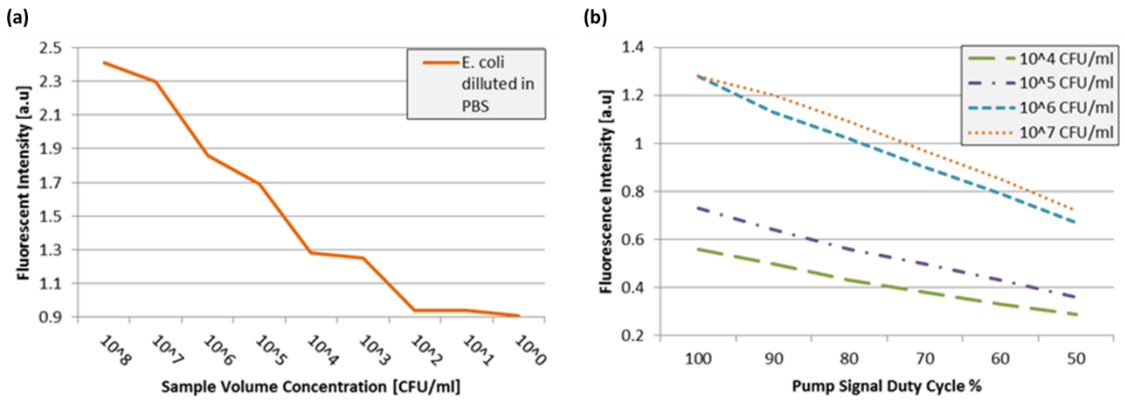

Figure 3.3: Dynamic range of concentrations detected with the device designed. (a) It is shown how 10^8 CFU/ml down to 10^2 CFU/ml concentrations can be distinguished and for lower microbiological charges (10 and 1 CFU/ml) an on and off response can be given. (b) Proves how varying the duty cycle in the PWM signal it is possible to assure the correct detection of a broad range of concentrations. Sample volumes from 10^7 CFU/ml down to 10^4 CFU/ml are shown on the graph mapping the pump intensity to the fluorescent emission intensity.

The fluorescently marked volume samples are prone to saturate or sub-saturate the detectors at the image sensor. In order to avoid this effect, a power controlled illumination source was implemented. The LED light source was driven by a pulse width modulation (PWM) signal. Figure 3.3 (b) demonstrates that by varying the duty cycle in the PWM signal from 100% to 50%, ultimately adapting the pump intensity, it is possible to assure the correct detection of a broad range of concentrations without saturation or sub-saturation. Sample volumes from 10^7 CFU/ml down to 10^4 CFU/ml are shown on the graph mapping the pump intensity in terms of duty cycle to the fluorescent emission intensity. For the lowest pump intensities it is possible to denote how all concentrations follow the same tendency towards sub-saturation; whereas for high pump power

the two highest concentrations (10^7 CFU/ml and 10^6 CFU/ml) saturate at the detector which makes them indistinguishable for processing.

Complexity and Size Analysis

Another capability of the system is the possibility to distinguish multiple populations within a single sample volume. This can be achieved in both non-fluorescent and fluorescently marked specimens. Figure 3.4 shows the resulting dispersion graphs of the detection of three sample volumes. The three volumes analyzed were known a priori to contain E. coli (10^6 CFU/ml), a sample with particles of multiple size (5µm up to 16µm) and a combined sample. The dispersion graph displays information linked to complexity and size of the particulate within the analyzed volumetric samples. From the graphs is possible to differentiate populations by mapping the detected particulate in a pure volume to part of the detected particulate in the mixed sample. (a) Displays the graph for non-fluorescent samples, while (b) displays the graphs for the same samples fluorescently marked with FITC.

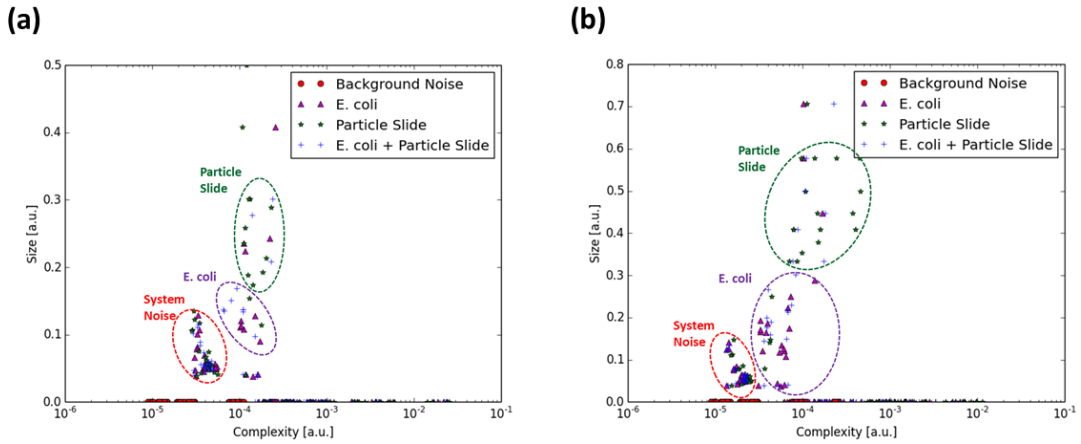

Figure 3.4: Dispersion graphs of the detection of three sample volumes. The three volumes analyzed were known a priori to contain E. coli (10^6 UFC/ml), a sample with particles of multiple size (5µm up to 16µm) and a combined sample. The dispersion graph displays information linked to complexity and size of the particulate within the analyzed volumetric samples. From the graphs is possible differentiate populations by mapping the detected particulate in a pure volume to part of the detected particulate in the mixed sample. (a) Displays the graph for non-fluorescent samples, while (b) displays the graphs for the same samples fluorescently marked with FITC.

3.4 Bordetella bronchiseptica and Streptococcus pneumonia Characterization

Two series of Streptococcus R6 (non-pathogenic) serialized 1ml samples were measured for concentrations 10^6 CFU/ml-10^1CFU/ml (without fluorescent markers). Furthermore, a PBS control sample of 1ml, which is a white sample (no microbiological charge). Also a particle slide of about 5µm in size was also captured for comparison purposes. Figure 3.5 displays the dispersion graphs containing data related to the complexity (horizontal axis) and size (vertical axis) of the detected sample. The graphs overlaps with the inherent background noise of the system. Note that size wise, a higher value represents a larger size; however in complexity, a broader range covered in the axis rather than a higher value represents more complex particulate. (a) Corresponds to a slide with particles of 5µm in size. (b), (c) and (d) correspond to a 1ml volume of a Streptococcus

dilution of one of the series with concentrations 10^6 CFU/ml, 10^5CFU/ml and 10^4CFU/ml respectively. Size wise, it is possible to characterize the region between 0.001 and 0.15 as the detected Streptococcus microorganisms. Figure 3.6 plot the microbiological charge or total count of the samples measured (both series). Sample 0 (left) corresponds to the particle slide used for calibration purposes, which consists of particles of 5µm in size. Series 1 (center) corresponds to the sample set decreasing logarithmically. The trend follows an increasing behavior from more concentrated (10^5 CFU/ml) to less concentrated (Control) samples. Series 2 (right) corresponds to the sample set decreasing logarithmically. The trend follows an increasing behavior from more concentrated (10^6 CFU/ml) to less concentrated (10^1 CFU/ml) samples. The increasing trend of the two measured series indicates that the measurements are repeatable.

Table 3.3 collects the information from the two series of captures represented in Figure 3.5. It shows the data for the Streptococcus R6 (non-pathogenic) serialized 1ml samples for concentrations 10^6 CFU/ml-10^1CFU/ml (without fluorescence markers), a PBS control sample of 1ml and a particle slide with 5µm beads. The microbiological charge (total count) indicates the concentration of particulates of interest in the 1ml sample. The trend follows an increasing behavior, from more concentrated to less concentrated samples; as expected. The target population indicates the ratio of presence of the microorganisms of interest with respect to other particulates present in the same sample and the background signal.

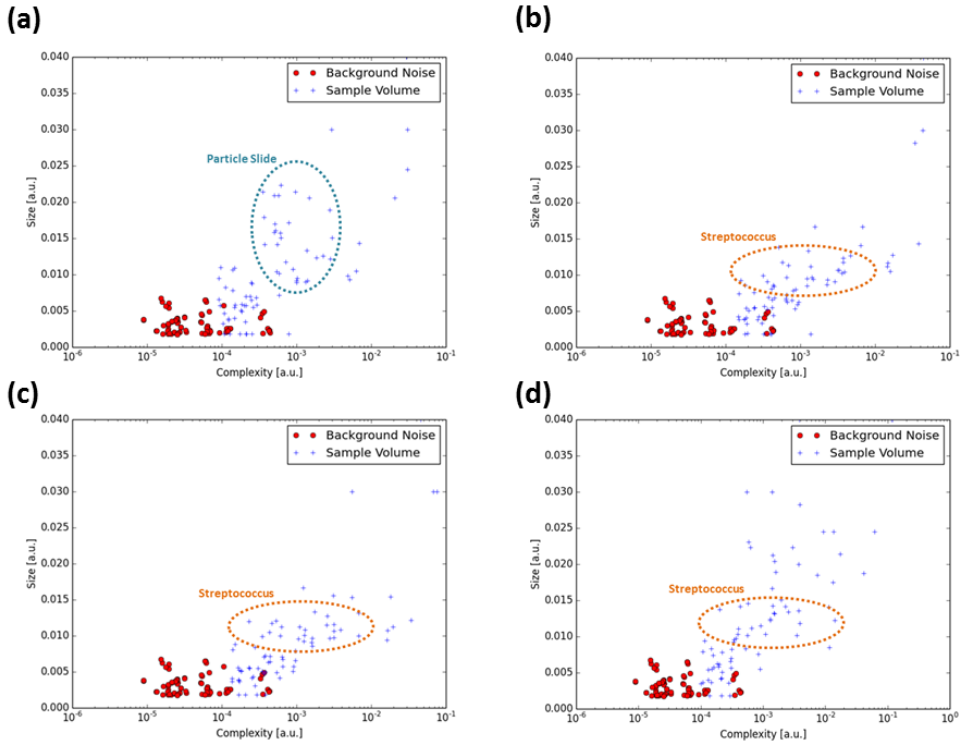

Figure 3.5: Dispersion graphs containing data related to the complexity (horizontal axis) and size (vertical axis) of the detected sample. The graphs overlaps with the inherent background noise of the system. Note that size wise, a higher value represents a larger size; however in complexity, a broader range covered in the axis rather than a higher value represents more complex particulate. (a) Corresponds to a slide with particles of 5µm in size. (b), (c) and (d) correspond to a 1ml volume of a Streptococcus dilution with concentration 10^6 CFU/ml, 10^5CFU/ml and 10^4CFU/ml respectively. Size wise, is possible to characterize the region between 0.001 and 0.15 as the detected Streptococcus microorganisms.

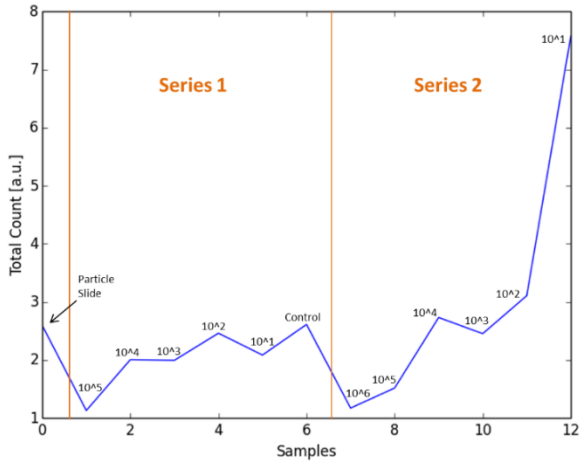

Figure 3.6: Microbiological charge (Total Count) of the samples measured. Sample 0 (left) corresponds to the particle slide used for calibration purposes, which consists of particles of about 5µm in size. Series 1 (center) corresponds to the sample set decreasing logarithmically. The trend follows an increasing behavior from more concentrated (10^5 UFC/ml) to less concentrated (Control) samples. Series 2 (right) corresponds to the sample set decreasing logarithmically. The trend follows an increasing behavior from more concentrated (10^6 UFC/ml) to less concentrated (10^1 UFC/ml) samples. Considering the two trend increasing trend of the two measured series, indicates that the measurements are repeatable.

Sample	Microbiological charge (total count)	Target population
Particle slide (5µm beads)	2.59	0.31
S1 10^5 CFU/ml	1.13	0.46
S1 10^4 CFU/ml	2.00	0.37
S1 10^3 CFU/ml	1.99	0.34
S1 10^2 CFU/ml	2.46	0.17
S1 10^1 CFU/ml	2.08	0.45
S2 10^6 CFU/ml	1.17	0.46
S2 10^5 CFU/ml	1.51	0.34
S2 10^4 CFU/ml	2.73	0.25
S2 10^3 CFU/ml	2.45	0.48
S2 10^2 CFU/ml	3.10	0.43
S2 10^1 CFU/ml	7.57	0.09
Control	2.61	0.31

Table 3.3: Two series of captures represented in Figure 3.5. It shows the data for the Streptococcus R6 (non-pathogenic) serialized 1ml samples for concentrations 10^6 CFU/ml-10^1CFU/ml (without fluorescence markers), a PBS control sample of 1ml and a particle slide with 5µm beads. The microbiological charge (total count) indicates the concentration of particulates of interest in the 1ml sample.

A differentiation study between Streptococcus and Bordetella bronchiseptica was also performed. Figure 3.7 is the dispersion graph showing the complexity and size data of the detected samples, where samples correspond to a 1ml volume of a Streptococcus, Bordetella and 50%/50% mix of Streptococcus and Bordetella, with 10^6 CFU/ml concentration. In the central part, delimited by the microbiological charge window (orange), the points indicate the statistical values of complexity and size. Furthermore, by counting the identified points of interest the microbiological charge is computed.

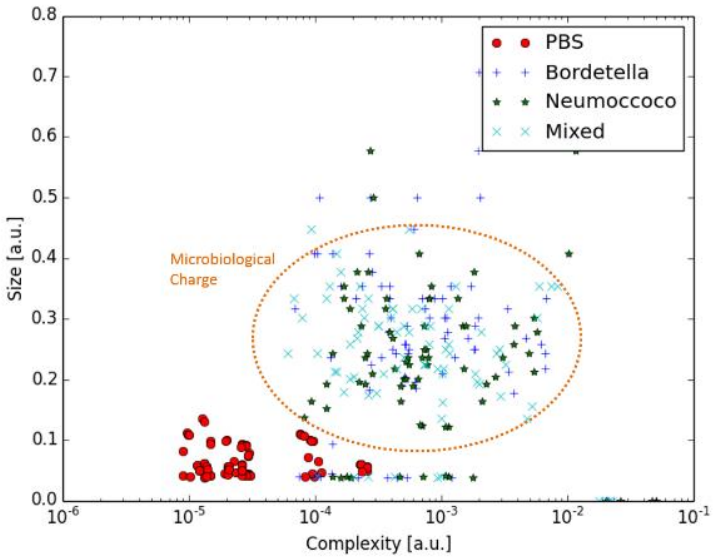

Figure 3.7: Dispersion graph containing the complexity and size data of the detected samples, where samples correspond to a 1ml volume of a Streptococcus, Bordetella and 50%/50% mix of Streptococcus and Bordetella, with 10^6 UFC/ml concentration. In the central part, delimited by the microbiological charge window (orange), the points indicate the statistical values of complexity and size. Furthermore, by counting the identified points of interest the microbiological charge is computed.

Concentration\Sample	Streptococcus microbiological charge (total count) [UFC/ml]	Bordetella bronchiseptica microbiological charge (total count) [UFC/ml]	Streptococcus + Bordetella bronchiseptica microbiological charge (total count) [UFC/ml]
S1 10^6 UFC/ml	3.74	2.79	3.18
S1 10^5 UFC/ml	4.20	3.88	3.95
S1 10^4 UFC/ml	4.45	5.03	3.67 (10% less concentration due to preparation)
S1 10^3 UFC/ml	16.44	13.78	13.26
S1 10^2 UFC/ml	16.33	13.01	14.21
S1 10^1 UFC/ml	3.82	3.70	4.23

Table 3.4: Three samples measured: Streptococcus R6 (non-pathogenic); Bordetella bronchiseptica and 50%/50% mixture of the latter two. The samples serialized 1ml samples for concentrations 10^6 UFC/ml-10^1UFC/ml (without fluorescence makers). The total count indicator increases for lower concentrations in bright field total microbiological charge count.

3.5 Jurkat Cells and K562 Cells (Lymphocyte and Granulocyte) Characterization

A common need in flow cytometry is the differentiation and characterization of human white blood cells. With this intention a set of captures of Jurkat and K562 cells were performed. Jurkat cells are T-lymphocytes, while K562 cells have a resemblance to granulocytes. The detection, characterization and concentration estimate of these type of cells may be useful on the diagnosis of several infectious diseases in humans. The series measured with the developed cytometer was composed as follows.

- Jurkat Cells (T lymphocyte)
  - Fluorescently marked with PerCP (Ex./Em.: 490nm/675nm)
  - Unmarked
- K562 Cells (Resemblance to granulocytes)
  - Fluorescently marked with FITC (Ex./Em.: 495nm/519nm)
  - Unmarked
- Jurkat + K562 Cells
  - Fluorescently marked with PerCP and FITC
  - Unmarked

All samples were provided in a 0.4ml dilution containing precisely 250.000 cells. They were further diluted in 0.6ml of PBS to obtain a sample volume of 1ml. The resulting dispersion graphs can be seen in Figure 3.8. In which the different populations can be identified. (a) Shows the results for the capture of the fluorescently marked specimens, using a dual band fluorescent filter appropriate for both emissions (PerCP and FITC); in it, is possible to identify the different populations within the sample volumes. (b) shows the equivalent results but for the unmarked sample volumes; also the distinction among population can be seen although to a lower degree than in the fluorescent application.

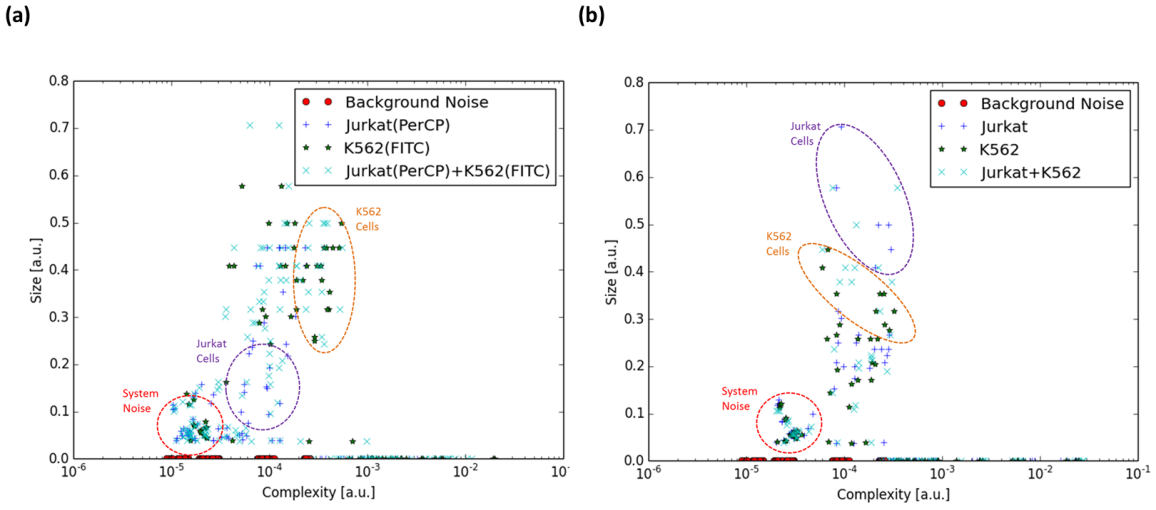

Figure 3.8: Resulting dispersion graphs. (a) Shows the results for the capture of the fluorescently marked specimens, using a dual band fluorescent filter appropriate for both emissions (PerCP and FITC); in it, is possible to identify the different populations within the sample volumes. (b) shows the equivalent results but for the unmarked sample volumes; also the distinction among population can be seen although to a lower degree than in the fluorescent application.

For concentration estimates a measure of the total count is made over the detected data. This total count implies information on the detected microbiological charge. It can be paired to a ratio on target population which relates the detected organisms over the noisy data, anything captured that is not considered to be the target specimen is then considered noisy data. Table 3.5 shows the measurements and calculations of microbiological charge and target population for each of the six sample volumes measured.

	Sample		Microbiological Charge (Total Count)	Target Population
CYT-F	Jurkat		16.34	0.26
	K562		34.73	0.31
	Mixed Volume	Jurkat	15.19	0.27
		K562	34.65	0.34
CYT-B	Jurkat		98.93	0.08
	K562		64.61	0.19
	Mixed Volume	Jurkat	84.97	0.11
		K562	75.33	0.12

Table 3.5: Measurements and calculations of microbiological charge and target population for each of the six sample volumes measured. The data displayed in the table comes from statistically analyzing the captured wave front patterns through its Fourier descriptor. Once the dispersion graph is obtained, the microbiological charge window is selected and with the statistical data, the total count and target ratio are calculated.

3.6 Fluidics

For environmental monitoring applications such as microbiological charge in water deposits, very large volumes (up to one liter) must be tested. The designed optical cytometer can only measure up to a few milliliters at a time. This said, a fluidic system was designed and implemented aiming at automated measurements of volumes larger than the capacity of the system. Using a computer control pressurized pump, the flow of the sample volume is managed to fill the chamber cavity of the cytometer, capture the sample and repeat the process iteratively until the entire sample volume has been measured. In order to improve the sensitivity of the cytometer for very low concentrations, a particulate concentrator is also added to the fluidic system; in this sense the sample volume is sequentially concentrated and measured.

Figure 3.9 displays the schematic of the fluidic system designed. A computer controlled pressurized pump (1) provides the exact air pressure (2) to commence the flow of the volume sample contained in the sealed vessel (3) through the fluidic system. The flowmeter (4) controls the rate at which the volume will be distribute along the system. A cell concentrator (5) passes

microbiologically charged fluid towards the measuring stage of the system and discards unpopulated fluid into the waste deposit (6). The concentrated volume fills the cytometer's chamber (7). Once the chamber is filled, the flow stops and the sample is measured. Next the pump and flowmeter restart the flow, the measured sample goes into a final container (8) and the chamber is refilled with the next volume to be captured.

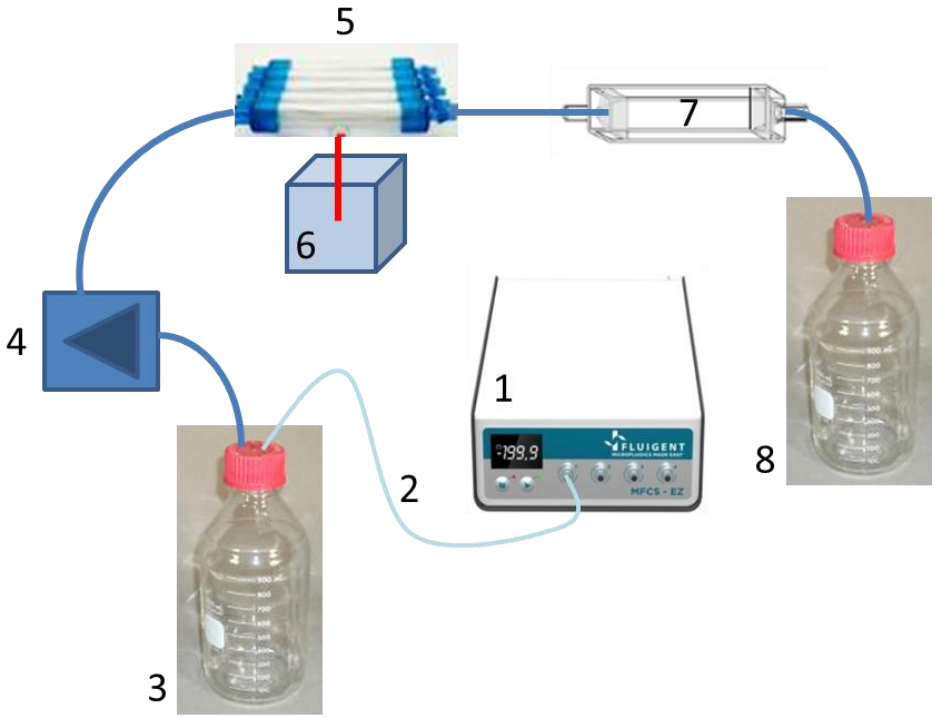

Figure 3.9: Schematic of the fluidic system designed. A computer controlled pressurized pump (1) provides the exact air pressure (2) to commence the flow of the volume sample contained in the sealed vessel (3) through the fluidic system. The flowmeter (4) controls the rate at which the volume will be distribute along the system. A cell concentrator (5) passes microbiologically charged fluid towards the measuring stage of the system and discards unpopulated fluid into the waste deposit (6). The concentrated volume fills the cytometer's chamber (7). Once the chamber is filled, the flow stops and the sample is measured. Next the pump and flowmeter restart the flow, the measured sample goes into a final container (8) and the chamber is refilled with the next volume to be captured.

Figure 3.10 shows the demo test of the fluidic system with emphasis on the cell concentrator, chamber cavity and the pressurized pump. (a) Displays the overall tested system. (b) Zooms into the cell concentrator (1) and the chamber cavity (2). (c) Displays the inside of the pressurized pump with four different pressure channels.

The system uses standard fluidic tubing which is easily replaced, as for the remaining components in the system they must be thoroughly clean to avoid contamination on future campaigns. The cleaning process consists on passing a volume of bleach through the system as to kill any remaining living particulate followed by a volume of ethanol to sterilize the materials.

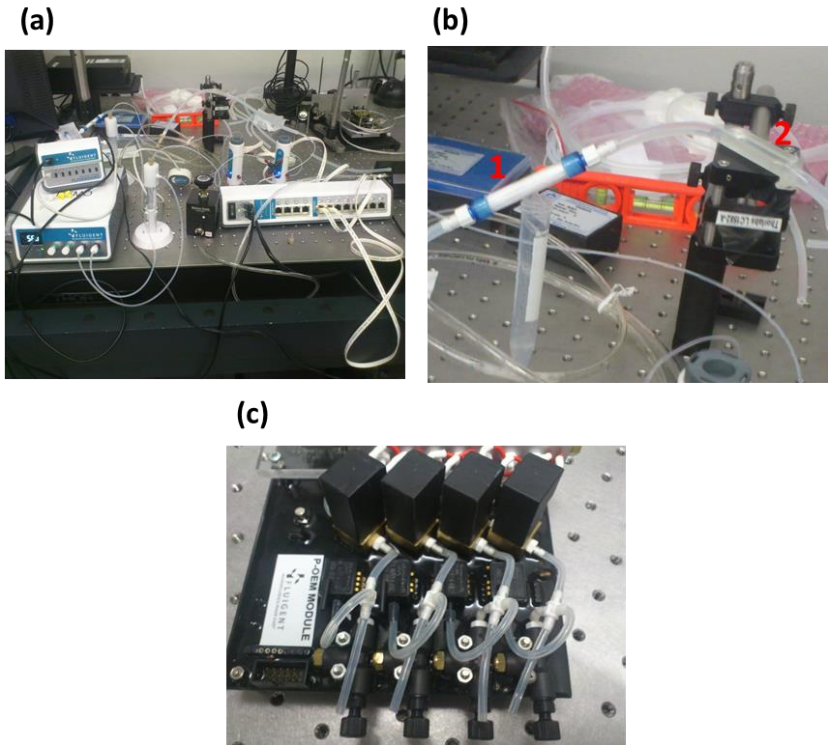

Figure 3.10: demo test of the fluidic system with emphasis on the cell concentrator, chamber cavity and the pressurized pump. (a) Displays the overall tested system. (b) Zooms into the cell concentrator (1) and the chamber cavity (2). (c) Displays the inside of the pressurized pump with four different pressure channels.

3.7 Summary

The pre-industrial prototype of the developed optical cytometer was proven effective for the detection and characterization of E. coli, streptococcus, Bordetella, Jurkat cells and K562 cells; with less than 30 minutes from sample preparation to final results. This implies it can be used in life sciences, including point of care applications in medical diagnosis, in environmental monitoring and food industry applications.

4 Conclusions

In this Thesis, an innovative image cytometer based on Fourier optics principles and capable of analyzing particulate in a volumetric sample has been designed, realized and characterized. In particular, a set of algorithms has been developed such that the luminescent wave front containing sample information can be captured and the data can be processed to retrieve information regarding size and complexity of the target specimen; ultimately with the goal of detecting, identifying and characterizing the particulate within the sample volume. The image cytometer has the capability of measuring sample volumes of up to a few milliliters due to the wide field of view and large depth or field provided by an ad-hoc opto-mechanical design. Furthermore, the device has a dual operation mode for both non-fluorescent and fluorescently marked samples and can deliver a result from sample preparation in less than thirty minutes. The detectable range of particulate concentration is compliant with the requirements of a wide range of applications, as it has been demonstrated with real biological samples containing Jurkat and K562 cells, streptococcus, Bordetella and E. coli microorganisms. The initial real setting experiments confirm the potential of the developed technology for medical diagnosis, environmental monitoring and food industry control.

Future immediate work will focus on optimizing the detection capabilities, measuring new particles, multiple populations and achieving a commercial product from the lab prototype of this thesis. This will be achieved by further developing the current optical design and software interface, to improve the image detection and increase the speed of information processing.

References

[1] H. Zhu, S. O. Isikman, O. Mudanyali, A. Greenbaum, and A. Ozcan, “Optical imaging techniques for point-of-care diagnostics,” *Lab Chip*, vol. 13, no. 1, pp. 51–67, Jan. 2012.

[2] S. Ah Lee, X. Ou, J. E. Lee, and C. Yang, “Chip-scale fluorescence microscope based on a silo-filter complementary metal-oxide semiconductor image sensor.,” *Opt. Lett.*, vol. 38, no. 11, pp. 1817–9, 2013.

[3] D. a. Buzatu, T. J. Moskal, A. J. Williams, W. M. Cooper, W. B. Mattes, and J. G. Wilkes, “An integrated flow cytometry-based system for real-time, high sensitivity bacterial detection and identification,” *PLoS One*, vol. 9, no. 4, p. e94254, Jan. 2014.

[4] P. Kozma, a. Lehmann, K. Wunderlich, D. Michel, S. Schumacher, E. Ehrentreich-Förster, and F. F. Bier, “A novel handheld fluorescent microarray reader for point-of-care diagnostic,” *Biosens. Bioelectron.*, vol. 47, pp. 415–420, Sep. 2013.

[5] H. Zhu, O. Yaglidere, T.-W. Su, D. Tseng, and A. Ozcan, “Cost-effective and compact wide-field fluorescent imaging on a cell-phone.,” *Lab Chip*, vol. 11, no. 2, pp. 315–322, Jan. 2011.

[6] P. Leonard, S. Hearty, J. Brennan, L. Dunne, J. Quinn, T. Chakraborty, and R. O’Kennedy, “Advances in biosensors for detection of pathogens in food and water,” *Enzyme Microb. Technol.*, vol. 32, no. 1, pp. 3–13, 2003.

[7] O. Lazcka, F. J. Del Campo, and F. X. Muñoz, “Pathogen detection: A perspective of traditional methods and biosensors,” *Biosens. Bioelectron.*, vol. 22, no. 7, pp. 1205–1217, Feb. 2007.

[8] B. Byrne, E. Stack, N. Gilmartin, and R. O’Kennedy, “Antibody-Based Sensors: Principles, Problems and Potential for Detection of Pathogens and Associated Toxins,” *Sensors*, vol. 9, no. 6, pp. 4407–4445, Jan. 2009.

[9] T. Publications, “(SAMPLE COPY , NOT FOR RESALE),” no. May, 2014.

[10] A. F. Coskun, I. Sencan, T.-W. Su, and A. Ozcan, “Wide-field lensless fluorescent microscopy using a tapered fiber-optic faceplate on a chip.,” *Analyst*, vol. 136, no. 17, pp. 3512–3518, Sep. 2011.

[11] A. F. Coskun, I. Sencan, T. W. Su, and A. Ozcan, “Lensfree fluorescent on-chip imaging of transgenic Caenorhabditis elegans over an ultra-wide field-of-view,” *PLoS One*, vol. 6, no. 1, p. e15955, Jan. 2011.

[12] H. Zhu, S. Mavandadi, A. F. Coskun, O. Yaglidere, and A. Ozcan, “Optofluidic fluorescent imaging cytometry on a cell phone,” *Anal. Chem.*, vol. 83, no. 17, pp. 6641–6647, 2011.

[13] D. Tseng, O. Mudanyali, C. Oztoprak, S. O. Isikman, I. Sencan, O. Yaglidere, and A. Ozcan, “Lensfree microscopy on a cellphone.,” *Lab Chip*, vol. 10, no. 14, pp. 1787–1792, Jul. 2010.

[14] R. S. Weinstein, M. R. Descour, C. Liang, G. Barker, K. M. Scott, L. Richter, E. a Krupinski, A. K. Bhattacharyya, J. R. Davis, A. R. Graham, M. Rennels, W. C. Russum, J. F. Goodall, P. Zhou, A. G. Olszak, B. H. Williams, J. C. Wyant, and P. H. Bartels, “An array microscope for ultrarapid virtual slide processing and telepathology. Design, fabrication, and validation study.,” *Hum. Pathol.*, vol. 35, no. 11, pp. 1303–14, Nov. 2004.

[15] M. Levoy, R. Ng, A. Adams, M. Footer, and M. Horowitz, “Light field microscopy,” *ACM Trans. Graph.*, vol. 25, no. 3, p. 924, 2006.

[16] M. Broxton, L. Grosenick, S. Yang, N. Cohen, K. Deisseroth, and M. Levoy, “Wave optics theory and 3-D deconvolution for the light field microscope,” vol. 21, no. 21, 2013.

[17] “The light field microscope,” vol. 24, no. 1996, p. 2006, 2006.

[18] G. Popescu, L. P. Deflores, J. C. Vaughan, K. Badizadegan, H. Iwai, R. R. Dasari, and M. S. Feld, “Fourier phase microscopy for investigation of biological structures and dynamics.,” *Opt. Lett.*, vol. 29, no. 21, pp. 2503–2505, 2004.

[19] F. Group, *IMAGE SENSORS and SIGNAL PROCESSING for DIGITAL*. 2006.

[20] D. L. Gilblom, S. Keun, and P. Ventura, “Operation and performance of a color image sensor with layered photodiodes,” vol. 5074, no. Figure 1, 2003.

[21] B. E. Bayer, “Color Imaging Array,” 3971065, 1976.

[22] P. M. Hubel and S. Clara, “Foveon Technology and the Changing Landscape of Digital Cameras.”

[23] C. Wootton, *A Practical Guide to Video and Audio Compression*. Elsevier, 2005.

[24] Photometrics, “Keep the Noise Down ! Low Noise : An Integral Part of High-Performance,” 2010.

[25] H. Tian, “Noise Analysisin CMOS Image Sensors,” Stanford University, 2000.

[26] T. I. Inc., “CCD IMAGE SENSOR NOISE SOURCES REFERENCE DOCUMENT,” 2012.

[27] M. W. D. Spring, Kenneth R., Thomas J. Fellers, “Introduction to Charge-Coupled-Devices (CCD).” [Online]. Available: http://www.microscopyu.com/articles/digitalimaging/ccdintro.html.

[28] D. Stoppa, “Emerging Research Topics in Advanced Solid-State Image Sensors,” no. September, 2012.

[29] D. Teledyne, “CCD vs CMOS. Which is better? It’s complicated.” [Online]. Available: http://www.teledynedalsa.com/imaging/knowledge-center/appnotes/ccd-vs-cmos/.

[30] A. Communications, “CCD and CMOS sensor technology,” 2010.

[31] “What is the difference between CCD and CMOS image sensors in a digital camera?” [Online]. Available: http://electronics.howstuffworks.com/cameras-photography/digital/question362.htm.

[32] P. Magnan, “Detection of visible photons in CCD and CMOS: A comparative view,” *Nucl. Instruments Methods Phys. Res. Sect. A Accel. Spectrometers, Detect. Assoc. Equip.*, vol. 504, no. 1–3, pp. 199–212, May 2003.

[33] R. Drivers, “CCD vs . CMOS : Choosing an imager means considering not only the chip , but,” no. January, 2001.

[34] J. Kuang, H. Yamaguchi, C. Liu, G. M. Johnson, and M. D. Fairchild, “Evaluating HDR rendering algorithms,” *ACM Trans. Appl. Percept.*, vol. 4, no. 2, p. 9–es, Jul. 2007.

[35] R. W. Picard and S. Mann, “Extending dynamic range by combining different exposed pictures,” *Proc. IS&T Ann. Conf.*, vol. 1, no. 2, pp. 442–448, 1995.

[36] T. Mitsunga and S. K. Nayar, “Radiometric self calibration,” *Proc. IEEE Comp. Vis. Patt. Recog.*, vol. 3, pp. 75–80, 1999.

[37] M. Robertson, S. Borman, and R. Stevenson, “Estimation-theoretic approach to dynamic range improvement using multiple exposures.,” *J. Elec. Imag.*, pp. 219–228, 2003.

[38] K. Kirk and H. J. Andersen, “Noise characterization of weighting schemes for combination of multiple exposures,” *Proc. Br. Mach. Vis. Conf.*, vol. 3, pp. 1129–1138, 2006.

[39] Paul E. Debevec and Jitendra Malik, “Recovering High Dynamic Range Radiance Maps from Photographs,” 1997.

[40] M. Granados, B. Ajdin, C. Theobalt, and H. P. A. Lensch, “Optimal HDR Reconstruction with Linear Digital Cameras,” vol. 1, no. 1.

[41] L. Melton, “The big picture,” *Nature*, vol. 437, no. September, 2005.

[42] S. O. Isikman, W. Bishara, S. Mavandadi, F. W. Yu, S. Feng, R. Lau, and A. Ozcan, “Lens-free optical tomographic microscope with a large imaging volume on a chip.,” *Proc. Natl. Acad. Sci. U. S. A.*, vol. 108, no. 18, pp. 7296–301, May 2011.

[43] M. B. Wakin, “An Introduction To Compressive Sampling,” *IEEE Signal Process. Mag.*, no. March, pp. 21–30, 2008.

[44] K. R. Spring and M. W. Davidson, “Introduction to Fluorescence Microscopy.” [Online]. Available: http://www.microscopyu.com/articles/fluorescence/fluorescenceintro.html.

[45] S. Weiss, “Fluorescence spectroscopy of single biomolecules.,” *Science*, vol. 283, no. 5408, pp. 1676–83, Mar. 1999.

[46] R. Lansford and S. E. Fraser, “Multi-Spectral Imaging and Linear Unmixing Add a Whole New Dimension to Laser Scanning Fluorescence Microscopy,” *BioImaging*, vol. 31, no. 6, 2001.

[47] “The Fluorescence Microscope.” [Online]. Available: http://www.nobelprize.org/educational/physics/microscopes/fluorescence/.

[48] J. R. Lakowicz, *Principles of Fluorescence Spectroscopy*. Springer Science & Business Media, 2007.

[49] N. Stuurman, “Fluorescence , Fluorescent microscopy and probes,” 2009.

[50] L. Song, E. J. Hennink, I. T. Young, and H. J. Tanke, “Photobleaching kinetics of fluorescein in quantitative fluorescence microscopy.,” *Biophys. J.*, vol. 68, no. 6, pp. 2588–600, Jun. 1995.

[51] P. R. Selvin, “The renaissance of fluorescence resonance energy transfer.,” *Nat. Struct. Biol.*, vol. 7, no. 9, pp. 730–4, Sep. 2000.

[52] J. W. Goodman, “Introduction to Fourier Optics McGraw-Hill Series in Electrical and Computer Engineering,” *Quantum Semiclassical Opt. J. Eur. Opt. Soc. Part B*, vol. 8, no. 5, p. 491, 1996.

[53] J. W. Miao, P. Charalambous, J. Kirz, and D. Sayre, “Extending the methodology of X-ray crystallography to allow imaging of micrometre-sized non-crystalline specimens,” *Nature*, vol. 400, no. 6742, pp. 342–344, 1999.

[54] X. C. Lectures, “Biological Imaging by X-ray Diffraction,” 2006.